Charge-Transfer Spectra and Bonding in Tetrahedral Mn^{VI}, Cr^{V}, and V^{IV} and Mn^{VII}, Cr^{VI}, and V^{V} Oxo Anions

M. Atanasov*

Institute of General and Inorganic Chemistry, Bulgarian Academy of Sciences, Bl.11, 1113 Sofia, Bulgaria

T. C. Brunold and H. U. Güdel

Department of Chemistry, University of Bern, Freiestrasse 3, CH-3000 Bern 9, Switzerland

C. Daul

Institut de Chimie Inorganique et Analytique, Universite de Fribourg Suisse, Perolles, CH-1700 Fribourg, Switzerland

Received August 13, 1997

Density functional theory (DFT) calculations on the tetrahedral Mn^{VI}, Cr^{V}, and $V^{IV}(d^1)$ oxo anions in their ground and lowest excited d−d and O → M charge transfer (CT) states are reported and used to assign the electronic absorption spectra by reference to the spectra of the isoelectronic Mn^{VII}, Cr^{VI}, and V^{V} (d^0) and the Mn^{V} and Cr^{IV} (d^2) anions. Calculated geometrical shifts along the totally symmetric metal−ligand vibration (α_1) for electronic excitations are in agreement with data deduced from experimental vibronic fine structures, supporting the proposed assignments. Using a CT model including (as different from DFT) configuration interaction (CICT), it is shown that the CT excited states of MnO_4^{2-} at 17 000, 23 300, and 28 200 cm^{-1} are due to d^2 $^3A_2(2e^2)$, $^1E(2e^2)$, and $^3A_2(2e^2)$ final states combining with a single hole ($\underline{L}$) on the ligand $1t_1$ and $4t_2$ orbitals, respectively. The higher $10Dq$ and smaller B values for the $d^2\underline{L}(d^1)$ states compared to those of the d^2 systems correlate with the shortening of the metal−ligand bond accompanying the removal of electrons from the antibonding d orbitals, leading to an increase in covalency and a change in the ordering of CT states for Cr^{V} with $^3T_2(2e^15t_2^1)\underline{L}$ ($10Dq$) at a higher energy than $^1E(2e^2)\underline{L}$ ($8B + 2C$) as compared to Cr^{IV} with nearly degenerate $^3T_2(2e^15t_2^1)$ and $^1E(2e^2)$ terms. This allows one to estimate the energy of the $^3A_2(2e^2)\underline{L} \rightarrow {}^1E(2e^2)\underline{L}$ transition from the CT ($d^2\underline{L}$) spectrum of $Cr^{V}(d^1)$, which could not be observed for Cr^{IV}. From a comparison of calculated and experimental oscillator strengths and Huang−Rhys factors (S) for the lowest CT band in the V^{V}, Cr^{VI}, and Mn^{VII} (d^0) and the V^{IV}, Cr^{V}, and Mn^{VI} (d^1) oxo anions, it is shown that the increase in covalency from left to right in this series is accompanied by a reduction in band intensity and S for the progression in the α_1 vibration. An explanation of this result in terms of ionic contributions to the metal−ligand bond increasing from Mn^{VI} to Cr^{V} and V^{IV} is proposed. Intensities of "d−d" transitions display the opposite trend; increasing covalency leads to stronger mixing between d → d and CT excited states and thus an increase in intensity.

I. Introduction

The interpretation of optical spectra of 3d metal complexes using ligand field (LF) models provides insight into metal−ligand bonding. Multiplets due to d^n configurations are strongly affected by ligand-to-metal charge transfer (CT) excited states, however, when going to transition metal ions in higher oxidation states such as the tetrahedrally oxo coordinated d^2 (Cr^{IV}, Mn^{V}, Fe^{VI}) and d^1 (V^{IV}, Cr^{V}, Mn^{VI}) ions, as was manifested by experimental[1−5] and recent theoretical[6,7] studies. The mixing of CT states into d^n multiplets leads to a violation from the prerequisites of LF models. This becomes increasingly pronounced with decreasing ligand-to-metal CT energy from left to right of the transition series and with increasing oxidation state of a given element.

In the studies thus far the effect of CT states has been studied indirectly by looking at their influence on the d^n manifold. CT bands in the electronic absorption spectra of d^2 ions are found at energies higher than 30 000 cm^{-1}, as in the case of Cr^{IV} and Mn^{V},[5] or are badly resolved, as in the case of Fe^{VI} [8] (overlapping

* Author to whom all correspondence should be addressed, at Institut de Chimie Inorganique et Analytique, Universite de Fribourg Suisse, Perolles, CH-1700 Fribourg, Switzerland.

(1) Hazenkamp, M. F.; Güdel, H. U.; Atanasov, M.; Kesper, U.; Reinen, D. *Phys. Rev. B* **1996**, *90*, 2367.
(2) Milstein, J. B.; Ackerman, J.; Holt, S. L.; McGarvey, B. R. *Inorg. Chem.* **1972**, *11*, 1178.
(3) Oetliker, U.; Herren, M.; Güdel, H. U.; Kesper, U.; Albrecht, C.; Reinen, D. *J. Chem. Phys.* **1994**, *100*, 8656.
(4) Brunold, T. C.; Hauser, A.; Güdel, H. U. *J. Lumin.* **1994**, *59*, 321.
(5) Reinen, D.; Rauw, W.; Kesper, U.; Atanasov, M.; Güdel, H. U.; Hazenkamp, M.; Oetliker, U. *J. Alloys Compd.* **1997**, *246*, 193 and references therein.
(6) Atanasov, M. *Chem. Phys.* **1995**, *195*, 49.
(7) Atanasov, M.; Adamsky, H.; Eifert, K. *J. Solid State Chem.* **1997**, *128*, 1.

S0020-1669(97)01014-8 CCC: $15.00
Published on Web 08/21/1998

d−d and CT bands prevent a detailed analysis of the CT spectral region). In this respect, the tetrahedral oxo anions V^{IV}, Cr^{V}, and Mn^{VI} play an exceptional role. On the one hand, because of the single d electron they possess a rather simple LF diagram with a ground state, $^2E(2e^1)$, and an excited state, LF $^2T_2(5t_2^1)$. On the other hand, highly resolved CT bands could be detected for MnO_4^{2-} (see refs 9 and 10) and also for CrO_4^{3-} and VO_4^{4-},[11] which are well separated from the single and less intense d−d band at lower energy (Figure 1a). While reported d−d band positions show minor changes between V^{IV}, Cr^{V}, and Mn^{VI}, CT transitions shift to lower energies from left to right of the transition series and show, in addition, nicely resolved fine structures. Energy band maxima, oscillator strengths, and Huang−Rhys parameters (S) for progressions in the totally symmetric metal−ligand stretching vibrations for the d^1 tetraoxo anions along with spectral data for the d^0 ions MnO_4^{-},[12] CrO_4^{2-},[13] and VO_4^{3-} [14] (Figure 1b) provide a good basis for a theoretical analysis.

Electronic structure calculations on the d^1 and d^0 oxo anions have been reported by many groups.[15−21] Surprisingly little effort has been made, however, to compare these data in order to deduce how chemical bonding changes with increasing oxidation state within the series of isoelectronic d^1 (V^{IV}, Cr^{V}, Mn^{VI}) and d^0 (V^{V}, Cr^{VI}, Mn^{VII}) ions or with addition of one extra electron to the 3d shell, from d^0 to d^1.

In this study, a combination of density functional theory (DFT) and a semiempirical model is used to deduce trends in metal−ligand bonding parameters of tetrahedral oxo anions. The intention of this paper is 2-fold:

(a) In a first step we report DFT calculations for the V^{IV}, Cr^{V}, and Mn^{VI} tetrahedral oxo anions focusing on the energies and equilibrium metal−oxygen bond distances for the LF $2e^1$-(3d) and $5t_2^1$(3d) and ligand-to-metal $d^2\underline{L}$ ($\underline{L}$: hole on the ligand) CT configurations and compare these with the corresponding CT $d^1\underline{L}$ (for the d^0) and LF configuration (for the d^2) oxo anions, respectively. Energies and compositions of the molecular orbitals (MOs) permit a comparison of the bonding in d^1 ions and their d^0 analogues, allowing the role of the extra electron in the 3d shell to be explored. The comparison will be in two directions (see Scheme 1): (i) along the series of isoelectronic d^0 (V^{V}, Cr^{VI}, Mn^{VII}) and d^1 (V^{IV}, Cr^{V}, Mn^{VI}) ions for a given electronic configuration and (ii) between $d^{n+1}\underline{L}$ CT excited states of d^n ions and LF states of d^{n+1} ions ($n = 0$ or 1). Energies and differences in the metal−ligand bond lengths of the various configurations are used to assign the bands in the absorption spectra, and the shapes and intensities of these bands are analyzed to explore metal−ligand covalency and ionicity.

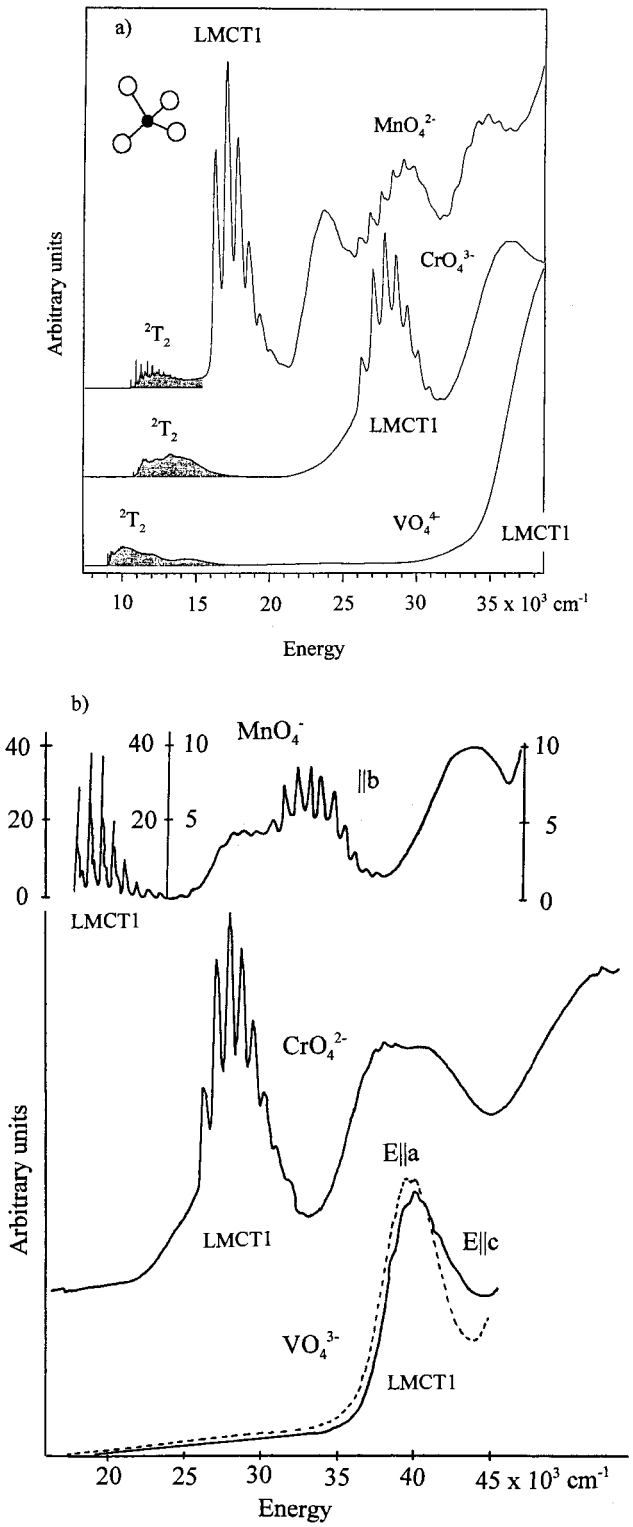

Figure 1. Arbitrarily scaled absorption spectra: (a) (top) MnO_4^{2-}-doped Cs_2SO_4 for $E\|a$, (middle) CrO_4^{3-}-doped Li_3PO_4, and (bottom) VO_4^{4-}-doped Mg_2SiO_4 for $E\|c$. The ligand-field (shaded areas) and the lowest energy ligand-to-metal CT bands are denoted by $^2T_2$ and LMCT1, respectively (adapted from T. Brunold, Ph.D. Thesis, Bern, 1996). (b) (top) $E\|b$ polarized absorption spectrum of $KMnO_4$ dissolved in $KClO_4$ at liquid helium temperature, adapted with permission from ref 12; (middle) absorption spectrum of Cr^{VI}-doped K_2SO_4 at 16 K, adapted with permission from ref 13; (bottom) $E\|a$ and $E\|c$ polarized absorption spectra of VO_4^{3-} in Ca_2PO_4Cl, adapted with permission from ref 14.

(8) Brunold, T. C.; Güdel, H. U.; Kück, S.; Huber, G. *J. Lumin.* **1996**, *65*, 293.
(9) (a) DiSipio, L.; Oleari, L.; Day. P. *J. Chem. Soc., Faraday Trans. 2* **1972**, *68*, 1972. (b) Day, P.; DiSipio, L.; Ingletto, G.; Oleari, L. *J. Chem. Soc., Dalton Trans.***1973**, 2595.
(10) Brunold, T. C.; Güdel, H. U.; Riley, M. J. *J. Chem. Phys.* **1996**, *105*, 7931.
(11) Brunold, T. C. Ph.D. Thesis, Bern, Switzerland, 1996, p 7.
(12) Holt, S. L.; Ballhausen, C. J. *Theor. Chim. Acta* **1967**, *7*, 313.
(13) Brunold, T. C.; Diploma Thesis, Bern, Switzerland, 1993, p 51.
(14) Borromei, R.; Ingletto, G. *Chem. Phys. Lett.* **1981**, *81*, 62.
(15) Johnson, K. H.; Smith, F. C., Jr. *Chem. Phys. Lett.* **1971**, *10*, 219.
(16) Ziegler, T.; Rauk, A.; Baerends, E. *J. Chem. Phys.* **1976**, *16*, 209.
(17) Nakai, H.; Ohmori, Y.; Nakatsuji, H. *J. Chem. Phys.* **1991**, *95*, 8287.
(18) Jitsuhiro, S.; Nakai, H.; Hada, M.; Nakatsuji, H. *J. Chem. Phys.* **1994**, *101*, 1029.
(19) Stückl, A. C.; Daul, C. A.; Güdel, H. U. *J. Chem. Phys.* **1997**, *107*, 4606.
(20) Deeth, R. J. *J. Chem. Soc., Faraday Trans*. **1993**, *89* (20), 3745.
(21) Deeth, R. J.; Sheen, P. D. *J. Chem. Soc., Faraday Trans.* **1994**, *90* (21), 3237.

Scheme 1

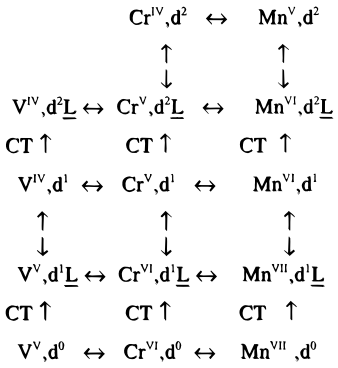

(b) In a second step a more refined treatment of CT transitions including multiplet structure will be given, using a configuration interaction charge-transfer model (CICT) with the ligand-to-metal CT energy (Δ), the cubic LF splitting ($10Dq$), and the Racah parameters of interelectronic repulsion (B, C) as model parameters. An assignment of band maxima to CT final states for the d^0 (V^V, Cr^{VI}, and Mn^{VII}) and d^1 (V^{IV}, Cr^V, and Mn^{VI}) ions, $d^1\underline{L}$ and $d^2\underline{L}$, respectively, is made, in close analogy with the analogous d^1 and d^2 ions. This allows changes in the equilibrium bond distances when moving from d^0 to d^1 and from d^1 to d^2 to be correlated with corresponding changes in the CT energies and LF parameters.

II. Theory

II.1. DFT Calculations. DFT calculations reported in this paper have been carried out with the Amsterdam Density Functional (ADF) program package (version 2.2).[22−26] The Vosko−Wilk−Nusair parametrization[27] of the electron gas data has been used for the exchange-correlation energy and potential. Density gradient corrections were included for the exchange[28] and for the correlation.[29] Triple-ζ Slater type orbitals (STOs), extended by a polarization function (TZP), were used for the metal atoms V, Cr, and Mn, where the core orbitals up to 2p were kept frozen. Oxygen atoms were described with a double-ζ STO basis, with the 1s orbital kept frozen. In the DFT calculations of all anions in this study, compensating positive charges have been used to ensure charge neutrality. In order to simulate the Madelung field and to counterbalance the excess negative charges, we have introduced four positive charges, +1, +0.75, and +0.5 at a distance of 1.78 Å behind the metal−oxygen bonds for VO_4^{4-}, CrO_4^{3-}, and MnO_4^{2-}, respectively. The distance 1.78 Å has been chosen to reproduce the Madelung energy per formula unit for K_2MnO_4 (309.23 eV) and was adopted without change for VO_4^{4-} and CrO_4^{3-}.[30] For all the anions, a geometry optimization for the ground and the lowest excited CT configurations was performed by varying the metal−ligand bond lengths while keeping the oxygen−positive point charge separation fixed (1.78 Å). In order to assess the role of ligand−ligand coupling and crystal field splitting effects on the ligand-based 2p orbitals, calculations have been performed on tetrahedral O_4^{8-} anions placed in an electrostatic field with positive charges Z_M at the center and q behind the O^{2-} anions: $Z_M(q) = +6$ (+0.5) for Mn^{VI}, +5 (+0.75) for Cr^V, and +4 (+1) for V^{IV}.

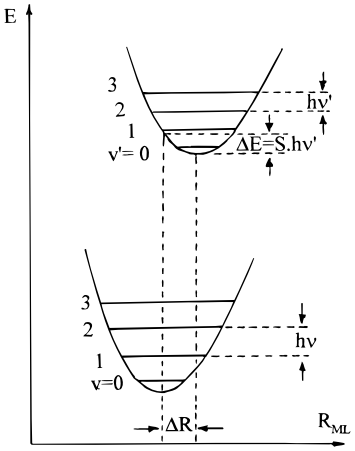

Figure 2. Potential energy curves and vibrational levels for the ground state and an excited state of a MO_4 cluster (schematic presentation). Vibrational frequencies and quantum numbers for the ground and the excited states are denoted by $h\nu$, υ and $h\nu'$, υ' respectively. The excited state energy stabilization (ΔE) and Huang−Rhys factor (S) are indicated.

From the calculated values of the total energies of the MO_4 model clusters, a fit to a quadratic polynomial ($a_2R_{ML}^2 + a_1R_{ML} + a_0$) yielded equilibrium bond lengths (R_0), totally symmetric harmonic force constants (K_{α_1}), and vibrational quanta ($h\nu$, $M = 16$: the reduced mass) of totally symmetric (α_1) vibrations for the $2e^1$ ground state configuration (eq 1). For the excited

$$R_0 = -a_1/2a_2$$

$$K_{\alpha_1}\,(\mathrm{cm}^{-1}/\text{Å}^2) = (1/2)a_2 \qquad (1)$$

$$h\nu = 1302.8[K_{\alpha_1}\,(\mathrm{mdyn/Å})/\mathrm{M})]^{1/2}$$

$$(1\ \mathrm{mdyn/Å} = 50\ 350\ \mathrm{cm}^{-1}/\text{Å}^2)$$

$5t_2^1$ and the ligand-to-metal CT configurations $d^2\underline{L}$, a considerable anharmonicity was observed and required the use of higher order polynomials to fit the calculated E vs R_{ML} plots. The Huang−Rhys factor $S_{\alpha 1}$, which relates to the difference in equilibrium metal−ligand bond length in the ground and excited states and equals the intensity ratio of the first sideband and the zero phonon line, is calculated from the vibrational relaxation energy ΔE of the excited state and the energy of its totally symmetric mode, $h\nu'$ (Figure 2):

$$S_{\alpha_1} = \Delta E/h\nu' \qquad (2)$$

II.2. Configuration Interaction CT Model for the d^0 (VO_4^{3-}, CrO_4^{2-}, MnO_4^-) and the d^1 (VO_4^{4-}, CrO_4^{3-}, MnO_4^{2-}) Anions. In this section, energies and equilibrium geometries of the relevant CT excited states are calculated in the tetrahedral approximation. Jahn−Teller (JT) modes leading to nuclear distortions along non totally symmetric coordinates

(22) Baerends, E. J.; Ellis, D. E.; Ros, P. *Chem. Phys.* **1973**, *2*, 41.
(23) Baerends, E. J.; Ros, P. *Int. J. Quantum Chem.* **1973**, *2*, 42.
(24) Baerends, E. J.; Ros, P. *Chem. Phys.* **1973**, *2*, 51.
(25) Boerrigter, P. M.; te Velde, G.; Baerends, E. J. *Int. J. Quantum Chem.* **1988**, *33*, 87.
(26) te Velde, G.; Baerends, E. J. *J. Comput. Phys.* **1992**, *99*, 84 and references therein.
(27) Vosko, S. H.; Wilk, L.; Nusair, N. *Can. J. Phys.* **1980**, *58*, 1200.
(28) Becke, A. D. *Phys. Rev. A* **1988**, *38*, 3098.
(29) Perdew, J. P. *Phys. Rev. B* **1986**, *33*, 8822.
(30) Choosing positive compensating charges has also the crucial effect of yielding positive ionization potentials as different to the bare anions for which in certain cases, such as MnO_4^{2-}, DFT predicts instability against ionization: $I_1(MnO_4^{2-}) = -3.35$ eV [but note the positive value of $I_1(MnO_4^-) = 5.9$ eV].

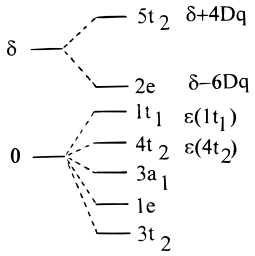

Figure 3. Orbital parameters for the $d^0 \rightarrow d^1\underline{L}$ and $d^1 \rightarrow d^2\underline{L}$ CT models of d^0 and d^1 tetrahedral MO_4 clusters. The ordering of MOs is the one deduced from DFT calculations for the ground states of MnO_4^-, MnO_4^{2-}, and CrO_4^{2-} (See section III.1.1 and Figure 4).

are neglected here, since the dominant progression-forming mode in the CT spectra (Figure 1) is the totally symmetric stretching mode.[31] For simplicity, the d^0 systems are considered first. A schematic energy level diagram is shown in Figure 3. The ligand 2p ($1t_1$, $4t_2$, $3a_1$, 1e, $3t_2$) and the metal 3d ($5t_2$, 2e) based MOs are centered at energies of 0 and δ, respectively. In the $^1A_1$ ground state, the fully occupied ligand-based MOs are below the unoccupied metal-based MOs. Excited state configurations are generated by transferring electrons from the 2p ($1t_1$, $4t_2$, $3a_1$, 1e, $3t_2$) ligand type into the 3d ($5t_2$, 2e) metal type MOs. From the many possible excitations, only electronic transitions from the strictly ($1t_1$) and approximately ($4t_2$) nonbonding orbitals need to be considered, as transitions from the lower lying 1e(π), $3t_2(\sigma+\pi)$, and $3a_1(\sigma)$ bonding orbitals of the 2p(O) type are calculated at much higher energies and are thus not observed (vide infra). For one-electron excitations from the $^1A_1(d^0)$ ground state, $^{1,3}T_1$ and $^{1,3}T_2$ CT excited states arise from $1t_1 \rightarrow$ 2e and $4t_2 \rightarrow$ 2e transitions and $^{1,3}A_{1(2)}$, $^{1,3}E$, $^{1,3}T_1$, and $^{1,3}T_2$ terms result from $4t_2(1t_1) \rightarrow 5t_2$ excitations, where only $^1A_1 \rightarrow {}^1T_2$ are spin and dipole allowed in T_d symmetry. Wave functions and the calculational procedure are described in Appendix I. Using these functions, diagonal energies, ΔE (measured from the $^1A_1$ energy), for each $^1T_2$ term and transition dipole matrix elements $D = \langle {}^1T_2|P_z|{}^1A_1\rangle$ (P_z is the z component of the dipole operator) can be derived (eq 3).

$$\Delta E(^1T_2,1t_1\rightarrow 2e) = \Delta - 6Dq - \epsilon(1t_1), \qquad D(2e\rightarrow 1t_1) = \sqrt{2}\langle v|P_z|g\rangle$$

$$\Delta E(^1T_2,4t_2\rightarrow 2e) = \Delta - 6Dq - \epsilon(4t_2), \qquad D(2e\rightarrow 4t_2) = -\sqrt{2}\langle u|P_z|z_L\rangle$$

$$\Delta E(^1T_2,1t_1\rightarrow 5t_2) = \Delta + 4Dq - \epsilon(1t_1), \qquad D(5t_2\rightarrow 1t_1) = -2\langle k|P_z|b\rangle$$

$$\Delta E(^1T_2,4t_2\rightarrow 5t_2) = \Delta + 4Dq - \epsilon(4t_2), \qquad D(5t_2\rightarrow 4t_2) = -2\langle k|P_z|e_L\rangle \quad (3)$$

Since the number of holes (10) is less than the number of electrons, we will use a hole notation in this section. The parameter Δ, which defines the ligand-to-metal CT energy as a difference between the baricenter energies of the $d^9\underline{L}$ and the d^{10} multiplets, can be expressed in terms of the orbital parameters (δ) and the Racah parameters of repulsion between holes, A, B, and C as shown in eq 4. $\epsilon(1t_1)$ and $\epsilon(4t_2)$ denote energies of ligand $1t_1$ and $4t_2$ orbitals.

$$\Delta = (d^9\underline{L}) - E(d^{10}) = \delta - 9A + 14B - 7C \qquad (4)$$

The cubic splitting parameter $10Dq$ accounts for both electrostatic and covalent (due to overlap between metal 3d and ligand 2s and 2p orbitals) contributions to the ligand field.

Let us now consider d^1 systems (corresponding to d^9 in the hole notation). Transferring one hole from the metal 2e and $5t_2$ to the $4t_2$ and $1t_1$ ligand orbitals ($d^9\rightarrow d^8\underline{L}$) will lead to a series of multiplets (45 states). Each of these states couples to 12 spin orbitals (hole on the $1t_1$ and $4t_2$ orbitals), leading to a total of 540 states. The problem becomes greatly simplified, however, if one restricts to doublet states only and uses symmetry arguments to obtain spin- and symmetry adapted functions (Appendix, Table A1). We list only terms ($^2T_1$ and $^2T_2$) for which transitions from the ground state (^2E) are allowed by the T_d dipole selection rules. Using these functions, diagonal energies and transition dipole matrix elements $D = \langle {}^2T_{2[1]}|P_z|{}^2E\rangle$ are derived (Appendix 1, Table A2).[32] As in the case of d^{10}, the parameter Δ defines the CT energy as a difference between the average energies of the CT $d^8\underline{L}$ and the ground state d^9 configurations (eq 5).

$$\Delta = E(d^8\underline{L}) - E(d^9) = \delta - 8A + 6B - 7C \qquad (5)$$

II.3. Dipole Transitions and Oscillator Strengths. Following refs 33 and 34, the intensity of CT transitions can be expressed in terms of matrix elements of the dipole operator between symmetry-adapted metal (3d) and ligand (2p) functions. Within this approximation matrix elements of the dipole operator between MOs are expressed as a linear combination of overlap integrals of functions centered at metal and ligand atoms. Overlap integrals between oxygen orbitals are calculated rather small, and ligand contributions to the metal 3d functions are neglected.[35] A discussion of the relative contributions of metal−ligand and ligand−ligand terms to the oscillator strengths of CT transitions and a description of the calculational procedure are provided in Appendix II.

III. Results and Discussion

III.1. Orbital and Bonding Scheme and M−O Bond Distances of d^0 (VO_4^{3-}, CrO_4^{2-}, MnO_4^-) and d^1 (VO_4^{4-}, CrO_4^{3-}, MnO_4^{2-}) Anions in Their Ground States. III.1.1. Orbital and Bonding Schemes. Valence orbital energies for the d^0 (VO_4^{3-}, CrO_4^{2-}, MnO_4^-) and d^1 (VO_4^{4-}, CrO_4^{3-},

(31) For a discussion of the JT effect in the ^2E ground state of V^{IV}, Cr^V, and Mn^{VI}, see: Atanasov, M. *Z. Phys. Chem.* **1997**, *200*, 57.

(32) In deriving the energies of the CT multiplets only repulsion between holes on the metal (on-site repulsion) was considered. Repulsion between metal and ligand holes, which is neglected here, leads to splitting between the $^2T_1$ and $^2T_2$ terms deriving from the same d^8 term when coupled to a given ligand hole. It has been shown that such integrals are rather small and, at least for transitions of the $1t_1$, $4t_2\rightarrow$2e and $4t_2\rightarrow 5t_2$ type, do not exceed 1500 cm^{-1}.[19] Therefore, in our model, pairs of states $^2T_2$ and $^2T_1$ stemming from the same $^{2S+1}\Gamma(d^8) - \underline{L}$ pair will be degenerate.

(33) Ballhausen, C. J.; Liehr, A. D. *J. Mol. Spectrosc.* **1958**, *2*, 342.

(34) Ballhausen, C. J. *Introduction to Ligand Field Theory*; McGraw Hill Book Co.: New York, 1962.

(35) This may be a severe approximation for more covalent metal−ligand bonds, as has been shown for $CuCl_4^{2-}$. In this case the amount of mixing of the ligand functions to the donor and acceptor MOs has been found to govern the intensity of CT bands: Ros, P.; Schuit, G. C. A. *Theor. Chim. Acta* **1966**, *4*, 1. van der Avoird, A.; Ros, P. *Theor. Chim. Acta* **1966**, *4*, 13. Solomon, E. I. *Comments Inorg. Chem.* **1984**, *3*, 227−320, see p 252, eq IV-2.

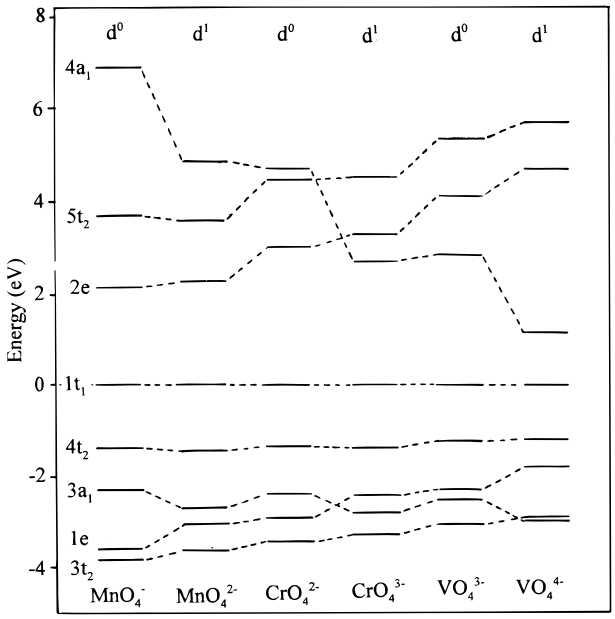

Figure 4. MO-level schemes obtained from DFT calculations on tetrahedral MO_4 clusters with the d^0 and d^1 electronic configurations M = Mn, Cr, and V ions in their $^1A_1(d^0)$ and $^2E(d^1)$ ground states, respectively. The $1t_1$ ligand nonbonding orbital is chosen as energy reference.

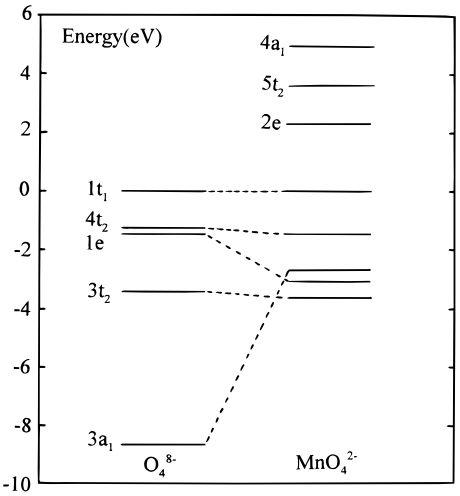

Figure 5. Energy diagram showing the correlation between DFT MOs of the O_4^{8-} cluster with charge +6 at the center and +0.5 behind the oxygen atoms (left) and MnO_4^{2-} (right). The geometrical arrangement of the O^{2-} ligands with respect to the charge-compensating point charges in O_4^{8-} and MnO_4^{2-} is according to the DFT optimized geometry for MnO_4^{2-}.

MnO_4^{2-}) oxo anions in their $^1A_1(d^0)$ and $^2E(d^1)$ ground states obtained from DFT calculations on the geometry optimized structures are plotted in Figure 4. The $1t_1$ MO is taken as the energy reference in Figure 4 as this is a pure ligand orbital. The metal−ligand bonding orbitals $3a_1(\sigma)$, $1e(\pi)$, and $3t_2(\sigma+\pi)$ are lower, while the antibonding $2e(\pi)$, $5t_2(\sigma+\pi)$, and $4a_1(\sigma)$ orbitals are higher in energy than $1t_1$. In order to explore the role of ligand−ligand interactions and crystal field splittings, calculations on separate O_4^{8-} clusters with the same geometry as the one for the MO_4 clusters have been performed with a point charge replacing the metal center. This is illustrated in Figure 5 for the case of MnO_4^{2-}. On going from O_4^{8-} to MnO_4^{2-}, the relative energies of $3t_2$, $4t_2$, and $1t_1$ do not change significantly. The $4t_2$ orbital for O_4^{8-} comprises σ and π contributions from the ligand $t_2(\sigma)$ and $t_2(\pi)$ MOs, initially

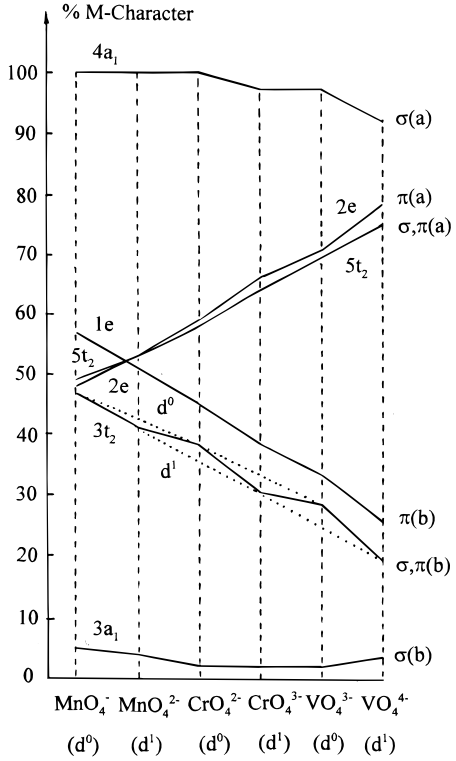

Figure 6. Metal orbital contributions (in %) to the MOs for tetrahedral MO_4 (M = Mn, Cr, V, d^0 and d^1) clusters. The bonding (b) and antibonding (a) character of each MO is indicated in parentheses.

suggesting that $4t_2$ is bonding with respect to Mn. These contributions are of different sign, however, and cancel almost completely in MnO_4^{2-}, resulting in an essentially nonbonding $4t_2$ ligand orbital. Note the large changes of energies of $3a_1$ and 1e from O_4^{8-} to MnO_4^{2-}: while 1e is stabilized due to metal−ligand bonding interactions of the π type, $3a_1$ increases in energy due to a decrease in ligand−ligand coupling.[36] A closer look at the MOs shows that the $3t_2$ orbital is stabilized by ligand−ligand overlap in O_4^{8-} but mostly by metal−ligand coupling in MnO_4^{2-}. As a result, its energy does not change much from O_4^{8-} to MnO_4^{2-}. The metal character in the relevant oxygen- and metal-based MOs is shown in Figure 6. Mixing between metal 3d and ligand 2p orbitals in the $3t_2$ and 1e MOs is rather strong, reflecting considerable metal−ligand covalency. It increases from d^1 to d^0 and from V to Cr and Mn: in this direction both 1e and $3t_2$ decrease in energy and become stronger bonding (Figure 4), which is reflected by their increasing metal contributions (Figure 6). The $4a_1$ orbital, mainly 4s in character, drops significantly in energy from left to right in Figure 4. This decrease is not unexpected: it is well-known that admixture of 4s to 3d orbitals of the same symmetry (such as d−s mixing in complexes with tetragonal and lower symmetries) increases from right to left in the transition metal series. However, the standard 4s(M) basis function used in our ADF calculations does overestimate this effect considerably. Thus for CrO_4^{3-} and VO_4^{4-}, $4a_1(4s)$ is calculated even lower than 2e(3d) (Figure 4), in contrast to spectroscopic data (see section III.2), which unambiguously show the reverse ordering. Artificial results due to anomalously low lying 4s orbitals, calculated using DFT, have been reported for RuO_4^{2-} [37] and linear oxometalate(I)

(36) The small metal character in the $3a_1$ orbital results from a small contribution from 4s in all clusters, possibly an artifact due to inappropriate 4s basis functions.

(37) Deeth, R. J. *J. Chem. Soc., Dalton Trans.* **1995**, 1537.

Table 1. Experimental Metal−Oxygen Bond Distances R_{ML} (in Å) for d^0 (VO_4^{3-}, CrO_4^{2-}, MnO_4^-) and d^1 (VO_4^{4-}, CrO_4^{3-}, MnO_4^{2-}) Oxo Anions in Their $^1A_1(d^0)$ and $^2E(d^1)$ Ground States and DFT Geometry Optimized Values

oxo anion	MnO_4^-	MnO_4^{2-}	CrO_4^{2-}	CrO_4^{3-}	VO_4^{3-}	VO_4^{4-}
calcd	1.638	1.674	1.668	1.710	1.717	1.769
exptl	1.629[a]	1.659[b]	1.660[c]	1.693[d]	1.708[e]	1.760[f]
comp	$KMnO_4$	K_2MnO_4	$(NH_4)_2CrO_4$	Sr_2CrO_4Cl	$Ba_3(VO_4)_2$	Sr_2VO_4

[a] Reference 43. [b] Reference 46. [c] Reference 42. [d] Reference 45. [e] Reference 41. [f] Reference 44.

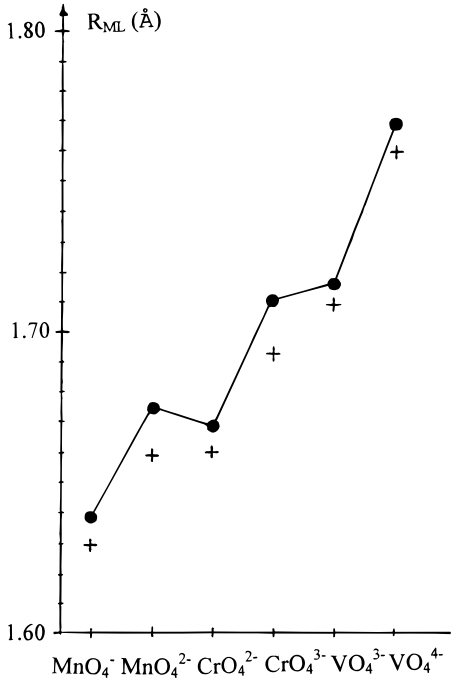

Figure 7. Metal−oxygen bond lengths in tetrahedral MO_4 clusters with M = Mn, Cr, and V ions in their $^1A_1$ (for d^0) and ^2E (for d^1) ground states as obtained from DFT geometry optimizations (●, calculated values) and from X-ray diffraction data (+, experimental values).

anions $[MnO_2]^{3-}$ (M = Cu, Ni, Co, Fe)[38] in sharp contrast to spectroscopic data (refs 39 and 40, respectively).

III.1.2. M−O Bond Distances. Experimental and DFT optimized M−O bond lengths (R_{M-O}) for the d^0 and d^1 tetraoxo anions in their $^1A_1(d^0)$ and $^2E(d^1)$ ground states are listed in Table 1 and plotted in Figure 7. Experimental M−O bond lengths[41−46] are very well reproduced by our calculations. The increase of the calculated metal−oxygen distances by 0.036 Å (for Mn), 0.042 Å (for Cr), and 0.052 Å (for V) when going from the d^0 to the d^1 systems reflects the weakening of the metal−ligand bond due to the additional antibonding 2e electron. Apparently, the magnitude of this antibonding interaction decreases with increasing covalency (decreasing ionicity, see below).

III.2. Excited-State Configurations and Electronic Absorption Spectra of d^0 (VO_4^{3-}, CrO_4^{2-}, MnO_4^-) and d^1 (VO_4^{4-}, CrO_4^{3-}, MnO_4^{2-}) Anions. In this section DFT calculated geometries and transition energies of the d^1 oxo anions will be compared to those of the d^0 anions. A more thorough analysis of the underlying multiplet structure will be carried out in section III.3. From section III.1 and previous work,[19] electronic transitions from the highest occupied $1t_1$ and $4t_2$ ligand orbitals to the 2e and $5t_2$ antibonding metal-based MOs dominate the CT spectrum, while the $2e \rightarrow 5t_2$ transition, formally a d−d transition, is responsible for the weak absorption band in the near-IR region (Figure 1a). Energy diagrams for the ground $2e^1$, lowest excited $2e \rightarrow 5t_2$ (formally d−d), and $1t_1 \rightarrow 2e$, $1t_1 \rightarrow 5t_2$, $4t_2 \rightarrow 2e$, and $4t_2 \rightarrow 5t_2$ CT configurations as a function of the metal−ligand bond distance (R_{ML}) for MnO_4^{2-}, CrO_4^{3-}, and VO_4^{4-} are presented in Figure 8. While equilibrium bond lengths R_{ML} only slightly increase from the π antibonding (^2E) ground state to the $\sigma + \pi$ antibonding $^2T_2$ LF excited state, CT excitations from nonbonding ligand orbitals to the antibonding 2e and $5t_2$ metal orbitals lead to a substantial increase in R_{ML}. This behavior becomes less pronounced with increasing covalency from VO_4^{4-} to CrO_4^{3-} to MnO_4^{2-}. Thus the calculated change of R_{ML} from the ground $2e^1$ to the lowest excited $1t_1 \rightarrow 2e$ CT configurations, which is as large as 0.087 Å in VO_4^{4-}, becomes 0.059 Å in CrO_4^{3-} and even smaller, 0.043 Å, in MnO_4^{2-}. This result is experimentally verified by the intensity distribution of the lowest CT absorption band (LMCT1) of CrO_4^{3-} and MnO_4^{2-} (Figure 1a). In both spectra the LMCT1 band exhibits a well-resolved vibrational progression in the totally symmetric stretching mode. However, the intensity distribution within the progressions is clearly different. The most intense member of the progression is the third one for CrO_4^{3-}; for MnO_4^{2-}, it is the second one. The same holds true for the corresponding d^0 anions, CrO_4^{2-} and MnO_4^-, respectively (Figure 1b). In line with our theoretical results, the increase of the metal−oxygen bond length upon LMCT1 excitation is considerably larger for CrO_4^{3-} than for MnO_4^{2-}, although the 2e orbital of MnO_4^{2-} is more antibonding and delocalized than that for CrO_4^{3-} (see section III.1).[47] Similar calculations have been carried out for the corresponding d^0 anions. A plot of equilibrium bond lengths for various configurations is given in Figure 9. The change in metal−ligand distance when moving from a given $d^1\underline{L}$ (d^0) to the corresponding $d^2\underline{L}$ (d^1) configuration provides a sensitive probe of metal−ligand bonding. The metal−ligand bond is weakened if an electron is added to the antibonding 2e or $5t_2$ d orbitals. The slopes of the lines connecting equilibrium bond distances for the $d^1\underline{L}$ (d^0) complexes and their $d^2\underline{L}$ (d^1) analogues increase slightly from Mn to Cr but considerably from Cr to V, indicating that this effect becomes stronger with increasing ionicity. Let us compare the bond lengths of the d^1 ions in their ^2E ground and $^2T_2$ excited states with those of the d^0 ions in their $1t_1 \rightarrow 2e$ and $1t_1 \rightarrow 5t_2$ CT excited states, respectively. With the exception of the extra hole on the $1t_1$ subshell these pairs of states are analogous. The equilibrium distances are indeed identical for $^2E(MnO_4^{2-})$ and $1t_1 \rightarrow 2e$ (MnO_4^-, $R_{ML} = 1.674$ Å) and comparable for $^2T_2$ (MnO_4^{2-}, $R_{ML} = 1.691$ Å) and $1t_1 \rightarrow 5t_2$ (MnO_4^-, $R_{ML} = 1.698$ Å). Proceeding to Cr and V, we observe some small yet non-negligible deviations: the bond lengths in the $1t_1 \rightarrow 2e$ excited states of the d^0 ions are longer

(38) Wang, S. G.; Schwarz, W. H. E. *J. Alloys Compds*. **1997**, *246*, 131.
(39) Brunold, T. C.; Güdel, H. U. *Inorg. Chem.* **1997**, *36*, 2084.
(40) Möller, A.; Hitchman, M. A.; Krausz, E.; Hoppe, R. *Inorg. Chem.* **1995**, *34*, 2684.
(41) Süsse, P.; Buerger, M. J. *Z. Krystallogr., Kristallgeomo, Kristallophys., Kristallchem.* **1970**, *131*, 161.
(42) Wells, A. F. *Structural Inorganic Chemistry*, 5th ed.; Oxford University Press: New York, 1986.
(43) Palenik, G. J. *Inorg. Chem.* **1967**, *6*, 503.
(44) Gong, W.; Greedan, J. E.; Liu, G.; Bjorgvinsson, M. *J. Solid State Chem.* **1991**, *94*, 213.
(45) Albrecht, C.; Cohen, S.; Mayer, I.; Reinen, D. *J. Solid State Chem.* **1993**, *107*, 218.
(46) Palenik, G. J. *Inorg. Chem.* **1967**, *6*, 507.

(47) This result is quite analogous to a recent ab initio calculation of the ground state ($^2E \times \epsilon$) Jahn−Teller couplings in the d^1 oxo anions (ref 31): with increasing covalency from VO_4^{4-} to CrO_4^{3-} and MnO_4^{2-}, the JT coupling strength and ground state geometric distortions seem to decrease. This point is still open to discussion, however.

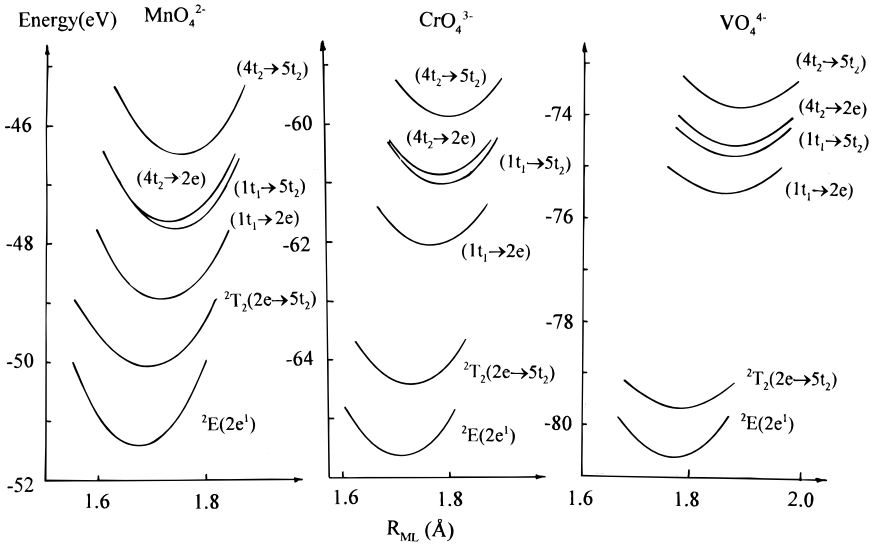

Figure 8. Potential energy curves for the ground and the lowest d−d (for d^1) and ligand-to-metal CT configurations of tetrahedral MO_4 (M = Mn, Cr, V, d^0 and d^1) model clusters as a function of the metal−oxygen bond distance R_{ML}.

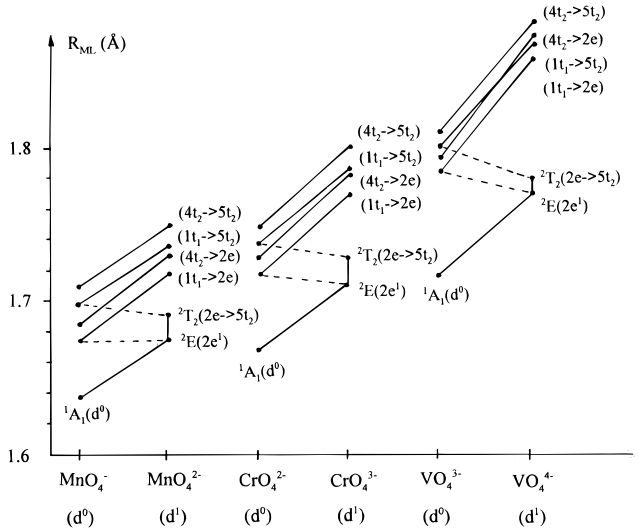

Figure 9. Equilibrium metal−oxygen bond lengths (R_{ML}) in the ground and the lowest excited d−d (for d^1) and ligand-to-metal CT configurations of tetrahedral MO_4 (M = Mn, Cr, V, d^0 and d^1) model clusters. The correlation between R_{ML} for electronic configurations of the d^0 ions with analogous ones for the d^1 ions, possessing one more electron in the π-antibonding 2e orbital, is represented by solid lines. The correlation berween the CT $d^1\underline{L}$ configurations of the d^0 ions with the ground (^2E) and excited ($^2T_2$) ligand field configurations of the d^1 ions is shown by dashed lines.

than those in the $^2E(d^1)$ ground state of the corresponding d^1 ions (dashed lines in Figure 9). These differences can be understood as follows. In the Mn complexes the excitations of the type $1t_1 \rightarrow 2e$ are to be regarded as a redistribution of electron density, rather than as proper ligand-to-metal CT transitions.[16] In the Cr and V complexes, however, the situation is different due to the higher ionicity of the metal−oxo bond (cf. the metal percentages to the MOs in Figure 6). An interesting correlation is found between the change in atomic charge and the increase in metal−ligand bond length (ΔR_{ML}) for the $1t_1 \rightarrow 2e$ and $1t_1 \rightarrow 5t_2$ (d^0) excitations (Table 2).[48] The larger the decrease of metal charge upon CT excitation, the larger the increase in ΔR_{ML}. In a simple ionic model, the energy (in eV) of an ionic pair, $U(R_{ML})$, with charges q_M and q_O is a sum of two terms: an attractive Coulomb term and a repulsive two-body term (eq 6), with D and n [$n = 7$, mean between $n =$ 5 (helium) and 9 (argon)] as parameters. Minimizing $U(R_{ML})$ with respect to R_{ML} (in Å) yields a minimum at $R_{ML}°$ (eq 7).

$$U(R_{ML}) = -14.4(q_M q_O/R_{ML}) + D/R_{ML}^{\,n} \qquad (6)$$

$$R_{ML}° = [nD/(14.4 q_M q_O)]^{1/(n-1)} \qquad (7)$$

As follows from eq 7 the metal−ligand bond gets longer with decreasing charges q_M and q_O upon CT excitation O → M. In support of this interpretation, the negative slopes of the dashed lines in Figure 9 become more pronounced with increasing ionicity from Cr to V. The same holds true for CT configurations including occupancy of the $5t_2$ orbital. Here ionic contributions seem more pronounced: even in the case of Mn, a small decrease of the R_{ML} bond distance from 1.698 Å ($1t_1 \rightarrow 5t_2$, d^0) to 1.691 Å ($^2T_2$, d^1) is calculated.

As follows from section III.1.1 (Figure 6) going from the d^0 complexes to their d^1 analogues, the mixing between metal 3d and ligand 2p orbitals in the bonding (antibonding) 1e (2e) MOs decreases. The same trend holds for the ground states of the d^0 (d^1) systems and the corresponding $d^1\underline{L}$ ($d^2\underline{L}$) CT states. Our calculations show that, upon $1t_1 \rightarrow 2e$ excitation, the 2e orbital increases in energy while the ligand character decreases (cf. Figures 4 and 6).[49]

A comparison of DFT calculated and experimental (where available) energies, equilibrium bond lengths, and vibrational energies of the totally symmetric M−O stretching mode (α_1) for the ground and relevant excited electronic configurations of the d^0 and d^1 oxo anions is given in Tables 3 and 4, respectively.[50] Calculated values for the energies of the lowest CT transitions compare reasonably well with the experimental values. Both sets of data show that the LMCT1 energies

(48) In Table 2 we use Voronoi charges which correspond, in essence, to charges calculated by integrating over Wigner−Seitz cells in solids.

(49) The increased 3d occupancy upon CT excitation might be very important for photochemical reactions. The metal−ligand bond becomes less covalent and is weakened as reflected by the longer M−O distances and the smaller energies of the M−O stretching mode for the excited states. In addition, the single electron on a $1t_1$ orbital may localize on a given O atom, and two such O radicals may combine to O_2. Thus interesting aspects emerge regarding the reactions, such as $KMnO_4 \rightarrow KMnO_2 + O_2$ and $2KMnO_4 \rightarrow KMnO_4 + MnO_2 + O_2$, whose mechanisms are not yet completely understood.

Table 2. Atomic Charges, q_M and q_O, Equilibrium Metal−Ligand Bond Lengths (R_{ML} in Å) for MnO_4^z d^0 Oxo Anions (M, z = Mn, −1; Cr, −2; V, −3, $^1A_1$ Ground State) and Their Changes (Δq_M, Δq_O, and ΔR_{ML}) upon $1t_1 \rightarrow 2e$ and $1t_1 \rightarrow 5t_2$ CT Excitation Calculated Using DFT

	$^1A_1$			$1t_1 \rightarrow 2e$			$1t_1 \rightarrow 5t_2$		
anion	R_{ML}	q_M	q_O	ΔR_{ML}	Δq_M	Δq_O	ΔR_{ML}	Δq_M	Δq_O
MnO_4^-	1.638	1.903	−0.726	0.036	−0.086	0.022	0.060	−0.109	0.027
CrO_4^{2-}	1.668	1.987	−0.997	0.049	−0.117	0.029	0.069	−0.129	0.032
VO_4^{3-}	1.717	2.047	−1.262	0.067	−0.396	0.099	0.083	−0.403	0.101

Table 3. Energies (in cm^{-1}), Equilibrium Metal−Ligand Bond Lengths (R_{ML} in Å), and Fundamental α_1 Mode Frequencies ($h\nu$, in cm^{-1}) for the Ground and Lowest Excited Ligand-to-metal CT Configurations of Tetrahedral MO_4^z (d^0) Oxo Anions (M, z = Mn, −1; Cr, −2; V, −3) with Compensating Positive Charges (DFT)[a]

config (transition)	ΔE		R_{ML}		$h\nu$		$S = \Delta E/h\nu$	
	calcd	exptl	calcd	exptl	calcd	exptl	calcd	exptl
			MnO_4^-.4(+0.25)					
ground state	0		1.638	1.629[b]	850	850[c]		
$1t_1 \rightarrow 2e$	19 082	19 000[e]	1.674		794	768[d]	1.02	1.73
$1t_1 \rightarrow 5t_2$	31 670	33 000[e]	1.698		775	760[d]	2.78	2.5
$4t_2 \rightarrow 2e$	30 003	28 500[e]	1.685		788		1.70	
$4t_2 \rightarrow 5t_2$	42 428	43 000[e]	1.709		747		4.03	
			CrO_4^{2-}.4(+0.5)					
ground state	0		1.668	1.66[f]	848	847[g]		
$1t_1 \rightarrow 2e$	27 167	27 030[h]	1.717		807	718[h]	1.86	3.6
$1t_1 \rightarrow 5t_2$	38 777	41 670[h]	1.737		761		3.85	
$4t_2 \rightarrow 2e$	37 577	36 360[h]	1.728		755	713[h]	2.70	3.6
$4t_2 \rightarrow 5t_2$	49 097		1.748		753		4.97	
			VO_4^{3-}.4(+0.75)					
ground state	0		1.717	1.708[i]	819	826[j]		
$1t_1 \rightarrow 2e$	37 827	39 500[k]	1.784		742	750[k]	3.55	≈5.0[k]
$1t_1 \rightarrow 5t_2$	47 134		1.800		736		5.21	
$4t_2 \rightarrow 2e$	47 142		1.794		733		4.46	
$4t_2 \rightarrow 5t_2$	56 442		1.810		693		6.66	

[a] Calculated and experimental Huang−Rhys parameters (S) for electronic transition from the ground state are also given. [b] Reference 43. [c] Miller, F. A.; Carlson, G. L.; Bentley, F. F.; Jones, W. H. *Spectrochim. Acta (London)* **1960**, *16*, 135. [d] Ballhausen, C. J. *Theor. Chim. Acta (Berlin)* **1963**, *1*, 285. [e] Reference 12. [f] Reference 42. [g] Stammreich, H.; Bassi, D.; Sala, O. *Spectrochim. Acta (London)* **1958**, *12*, 403. [h] Reference 59. [i] Reference 41. [j] Gonzalez-Vilchez, F.; Griffith, W. P. *J. Chem. Soc., Dalton Trans.* **1972**, 1416. [k] Reference 14.

decrease from the left (V) to the right (Mn) of the isoelectronic transition series and to a lesser extent from the d^1 to the d^0 anions. It should be noted, however, that the energy of this transition is greatly affected by the surroundings. For example for VO_4^{3-} it is observed at 39 500 cm^{-1} in Ca_2PO_4Cl,[14] at 36 500 cm^{-1} in aqueous alkaline (1 M NaOH) solution,[51] and at 24 000 cm^{-1} in SiO_2 codoped with Al^{III}.[52] For the d^0 systems, there is good agreement between experimental and calculated transition energies, although the values for $1t_1 \rightarrow 5t_2$ and $4t_2 \rightarrow 2e$ are too close in energy. Further, ground state vibrational energies for the α_1 stretching mode compare nicely with the experimental values. In the CT excited states the energy of this vibration is reduced, where this effect becomes more pronounced from Mn to Cr and V. In the order of increasing energy, the CT absorption bands of the d^0 ions can be assigned to $1t_1 \rightarrow 2e$, $4t_2 \rightarrow 2e$, $1t_1 \rightarrow 5t_2$, and $4t_2 \rightarrow 5t_2$ excitations, in agreement with DFT calculations reported recently[19] but in variance with previous assignments for MnO_4^- [12,17] and CrO_4^{2-}.[18]

It is generally accepted that the LMCT1 band (Figure 1b) in all cases is due to the allowed $^1A_1 \rightarrow {}^1T_2$ ($1t_1 \rightarrow 2e$) transition. This proposal is supported by the good correspondence between calculated and experimental S_{α_1} values (Table 3) for MnO_4^- and VO_4^{3-} but not for CrO_4^{2-}. Apparently, the approximation of an isolated cluster seems not to work quite well in this case (see below). In refs 12 and 17 the nicely resolved band at 33 000 cm^{-1} of MnO_4^- has been assigned to the $^1A_1 \rightarrow {}^1T_2$ ($4t_2 \rightarrow 2e$) transition. In view of the calculated Huang−Rhys parameters (Table 3) we reassign this band to $1t_1 \rightarrow 5t_2$ (see also next section). While the calculated values for the oscillator strengths differ substantially from the experimental values (see the approximations inherent in section II.3), they do, however, reproduce the experimental trend: a decrease from VO_4^{3-} to CrO_4^{2-} and MnO_4^-. This indicates that, as the metal bond becomes more covalent, the LMCT1 transition loses intensity. In the same order the Huang−Rhys factors (S) for the α_1 stretching modes decrease (see Table 3).

For the d^1 systems MnO_4^{2-}, CrO_4^{3-}, and VO_4^{4-}, direct comparison of the calculated and experimental data (Table 4) is complicated due to the multiplet structure arising from CT excited configurations (formally d^2 metal ions) which is not accounted for in our DFT calculations. Nevertheless, the calculations allow trends to be explored. Similar to the d^0 complexes, the calculated Huang−Rhys parameter S_{α_1} for the lowest CT transition ($1t_1 \rightarrow 2e$) increases significantly from Mn to Cr and V, consistent with experimental data (Table 4). DFT calculated values for $10Dq$ decrease from MnO_4^{2-} (10 792 cm^{-1}) to CrO_4^{3-} (9872 cm^{-1}) and VO_4^{4-} (7736 cm^{-1}). While the calculations appear to underestimate $10Dq$, it is important

(50) From parallel calculations on the bare and the charge-compensated clusters, better agreement between calculated and experimental ground state bond lengths was obtained for the neutral clusters compared to the bare oxo anions. Introducing positive charges also leads to a shift of the doubly occupied ligand 2p-type and empty metal 4s-type MOs to lower and higher energies, respectively. This could explain why in DFT calculations on negatively charged molecules the empty 4s orbital is frequently placed below occupied 3d orbitals. Thus a calculation which exaggerates the surrounding positive charges for VO_4^{4-} causes a change of the order of orbitals in Figure 4 to the expected one: $2e < 5t_2 < 4a_1$. Another reason for this may be inappropriate basis sets used to describe virtual 4s orbitals (see section III.1.1).

(51) Muller, A.; Diemann, E.; Ranade, A. C. *Chem. Phys. Lett.* **1969**, *3*, 467.

(52) Blasse, G. *Structure Bonding (Berlin)* **1980**, *42*, 1-41.

Table 4. Energies (in cm^{-1}), Equilibrium Metal−Ligand Bond Lengths (R_{ML} in Å), and Fundamental α_1 Mode Frequencies ($h\nu$, in cm^{-1}) for the Ground and Lowest Excited (Ligand Field and Ligand-to-Metal CT) Configurations of Tetrahedral MO_4^z (d^1) Oxo Anions (M, z = Mn, −2; Cr, −3; V, −4) with Compensating Positive Charges (DFT)[a]

config (transit)	ΔE calcd	ΔE exptl	R_{ML} calcd	R_{ML} exptl	$h\nu$ calcd	$h\nu$ exptl	$S = \Delta E/h\nu$ calcd	$S = \Delta E/h\nu$ exptl
			MnO_4^{2-}.4(+0.5)					
ground state		0	1.674	1.65[b]	824	812[c]		
$2e \rightarrow 5t_2$	10 792	12 000[d]	1.691		755	778[e]	0.21	0.5[d]
$1t_1 \rightarrow 2e$	20 653	17 000[d]	1.717		810		1.41	1.60[e]
		23 300[d]						
$1t_1 \rightarrow 5t_2$	31 440		1.735		823		2.94	
$4t_2 \rightarrow 2e$	32 086	28 200[d]	1.729		801		2.34	2.60
		34 200[d]						
$4t_2 \rightarrow 5t_2$	42 760		1.748		817		4.21	
			CrO_4^{3-}.4(+0.75)					
ground state		0	1.709_5	1.695 [f]	799	817[g]		
$2e \rightarrow 5t_2$	9 872	13 500[d]	1.728		782		0.25	
$1t_1 \rightarrow 2e$	30 475	28 000[d]	1.769		726		2.34	2.6
		36 000[d]						
$1t_1 \rightarrow 5t_2$	40 319		1.786		781		4.27	
$4t_2 \rightarrow 2e$	41 061		1.784		736		3.73	
$4t_2 \rightarrow 5t_2$	50 651		1.800		742		5.72	
			VO_4^{4-}.4(+1.0)					
ground state		0	1.769	1.76[i]	777	818[c]		
$2e \rightarrow 5t_2$	7 736	10 400[h]	1.781		780	755[h]	0.11	0.90
$1t_1 \rightarrow 2e$	44 687	>37 000[h]	1.856		641		5.30	
$1t_1 \rightarrow 5t_2$	51 305		1.867		660		6.24	
$4t_2 \rightarrow 2e$	53 406		1.872		669		6.80	
$4t_2 \rightarrow 5t_2$	60 096		1.880		658		8.03	

[a] Calculated and experimental Huang−Rhys parameters (S) for electronic transition from the ground state are also given. [b] Reference 46. [c] Gonzalez-Vilchez, F.; Griffith, W. P. *J. Chem. Soc., Dalton Trans.* **1972**, 1416. [d] Reference 11. [e] Reference 10. [f] Reference 45. [g] Reference 63. [h] Reference 56. [i] Reference 44.

to note that the experimental $10Dq$ values show a strong dependence on the host lattice.[53,54] For example, $10Dq$ values reported for VO_4^{4-} doped into Mg_2GeO_4, Ca_2GeO_4, and Mg_2SiO_4 are ≅9000,[55] 10 400, and 12 000 cm^{-1},[56] respectively [ionic radii are 0.41 Å (V^{IV}),[57] 0.39 Å (Ge^{IV}),[58] and 0.26 Å (Si^{IV})[58]].

III.3. Configuration Interaction Charge Transfer (CICT) Model Calculations for the d^0 (VO_4^{3-}, CrO_4^{2-}, MnO_4^-) and d^1 (VO_4^{4-}, CrO_4^{3-}, MnO_4^{2-}) Oxo Anions. In this section the electronic spectra of the d^0 (VO_4^{3-}, CrO_4^{2-}, MnO_4^-) and d^1 (VO_4^{4-},CrO_4^{3-}, MnO_4^{2-}) oxo anions are analyzed using the CICT model introduced in section II.2. In contrast to the DFT formalism, this model takes into account configuration interaction between multiplets. Band assignments for the d^0 complexes MnO_4^- (in $KClO_4$[12]) and CrO_4^{2-} (in $3CdSO_4 \cdot 8H_2O$[59]), derived using the CICT model, are given in Table 5 together with the relevant data of their d^1 analogues.[60] From the experimental transition energies, values for $10Dq = \epsilon(5t_2) - \epsilon(2e)$ and the energy splitting, $\epsilon(1t_1) - \epsilon(4t_2)$, can be calculated as differences between the energies of two pairs of transitions (eq 8). From

$$10Dq = \Delta E(1t_1 \rightarrow 5t_2) - \Delta E(1t_1 \rightarrow 2e) = \Delta E(4t_2 \rightarrow 5t_2) - \Delta E(4t_2 \rightarrow 2e)$$

$$\epsilon(1t_1) - \epsilon(4t_2) = \Delta E(1t_1 \rightarrow 2e) - \Delta E(4t_2 \rightarrow 2e) = \Delta E(1t_1 \rightarrow 5t_2) - \Delta E(4t_2 \rightarrow 5t_2) \quad (8)$$

Table 5, $\epsilon(1t_1) - \epsilon(4t_2)$ and $10Dq$ do not significantly change from MnO_4^- to CrO_4^{2-}. The decrease of $10Dq$ from MnO_4^- (14 000 cm^{-1}) to MnO_4^{2-} (12 000 cm^{-1}) and from CrO_4^{2-} (14 640 cm^{-1}) to CrO_4^{3-} (13 500 cm^{-1}) reflects the increase of the ground state R_{ML} distance due to occupancy of the antibonding 2e orbital.

Table 5. Band Maxima (in cm^{-1}) in the Electronic Absorption Spectra of Tetrahedral MnO_4^- and CrO_4^{2-} (d^0) Oxo Anions and Values of $10Dq(d^1\underline{L})$ and $\epsilon(1t_1) - \epsilon(4t_2)$ (in cm^{-1}) Deduced from CICT Model[a]

transition [energy expression]	MnO_4^-	CrO_4^{2-}
$1t_1 \rightarrow 2e$ $[\Delta - 6Dq - \epsilon(1t_1)]$	19 000[b]	27 030[c]
$4t_2 \rightarrow 2e$ $[\Delta - 6Dq - \epsilon(4t_2)]$	28 500[b]	36 360[c]
$1t_1 \rightarrow 5t_2$ $[\Delta + 4Dq - \epsilon(1t_1)]$	33 000[b]	41 670[c]
$4t_2 \rightarrow 5t_2$ $[\Delta + 4Dq - \epsilon(4t_2)]$	43 000[b]	
$10Dq(d^1\underline{L})$	14 000	14 640
$\epsilon(1t_1) - \epsilon(4t_2)$	10000	9 330
$R_{ML}(d^0)$	1.629	1.66
$10Dq(d^1)$	12 000	13 500
$R_{ML}(d^1)$	1.65	1.695

[a] For a comparison, values of $10Dq$ (in cm^{-1}) and R_{ML} (equilibrium metal−oxygen bond lengths, in Å) for the d^1 ions (MnO_4^{2-}, CrO_4^{3-}) are also given. [b] Reference 12. [c] Reference 59.

(53) (a) Reinen, D.; Lachwa, H.; Allmann, R. *Z. Anorg. Allg. Chem.* **1986**, *542*, 71. (b) Reinen, D.; Lachwa, H. *Inorg. Chem.* **1989**, *28*, 1044.
(54) Atanasov, M.; Adamsky, H.; Reinen. D. *Chem. Phys.* **1996**, *202*, 155.
(55) Rauw, W. Ph.D. Thesis, Marburg, Germany, 1997.
(56) Brunold, T. C.; Güdel, H. U.; Kaminskii, A. A. *Chem. Phys. Lett.* **1997**, *271*, 327.
(57) Calculated from the V^{IV}−O bond length (1.76 Å) and $r(O^{2-}) = 1.35$ Å.
(58) Shannon, R. D. *Acta Crystallogr. A* **1976**, *32*, 751.
(59) Murthy, T. S. N.; Ramalingaiah, S.; Reddy, K. N.; Salagram, M. *Solid State Commun.* **1986**, *60*, 715.
(60) An alternative assignment of the 28 500 and 33 000 cm^{-1} bands in MnO_4^- as $1t_1 \rightarrow 5t_2$ and $4t_2 \rightarrow 2e$ transitions, respectively (as proposed in ref 18 and ref 12 for the latter transition), would result in a value of $10Dq$ (9500 cm^{-1}), which is too low when compared to the one for MnO_4^{2-} (12 000 cm^{-1}). This, as well as the calculated $S_{\alpha 1}$ values (section III.2), supports the assignment in Table 5.

Table 6. Band Assignments, Calculated (Using CICT Model), Experimental Transition Energies (in cm^{-1}), and Oscillator Strengths for MnO_4^{2-}

excited state (electronic transition)	diagonal energy	transition energy		oscillator strength	
		calcd[a]	exptl	calcd	exptl
$^2T_2$ ($2e \rightarrow 5t_2$)	$10Dq$	12 000	12 000	0.0004[b]	0.001
$^2T_2(1t_1,a^3A_2)$ ($1t_1 \rightarrow 2e$)	$\Delta - 6Dq - \epsilon(1t_1)$	17 000	17 000	0.006	0.024
$^2T_{2[1]}(1t_1,a^1E)$ ($1t_1 \rightarrow 2e$)	$\Delta - 6Dq + 8B + 2C - \epsilon(1t_1)$	23 300	23 300	0.011	0.022
$^2T_{2[1]}(1t_1,^3T_2)$ ($1t_1 \rightarrow 5t_2$)	$\Delta + 4Dq - \epsilon(1t_1)$	28 200	28 200	0.0	
$^2T_{2[1]}(1t_1,a^1A_1)$ ($1t_1 \rightarrow 2e$)	$\Delta - 6Dq + 16B + 4C - \epsilon(1t_1)$	27 914	28 200	0.003	
$^2T_1(4t_2,^3A_2)$ ($4t_2 \rightarrow 2e$	$\Delta - 6Dq - \epsilon(4t_2)$	28 200	28 200	0.026	0.028
$^2T_{2[1]}(1t_1,a^3T_1)$ ($1t_1 \rightarrow 5t_2$)	$\Delta + 4Dq + 12B - \epsilon(1t_1)$	32 174		0.0	
$^2T_{2[1]}(4t_2,a^1E)$ ($4t_2 \rightarrow 2e$)	$\Delta - 6Dq + 8B + 2C - \epsilon(4t_2)$	34 200	34 200	0.021	0.020
$^2T_{2[1]}(4t_2,^3T_2)$ ($4t_2 \rightarrow 5t_2$)	$\Delta + 4Dq - \epsilon(4t_2)$	39 400		0.0	
$^2T_2(4t_2,a^1A_1)$ ($4t_2 \rightarrow 2e$)	$\Delta - 6Dq + 16B + 4C - \epsilon(4t_2)$	39 114		0.012	
$^2T_{2[1]}(4t_2,a^3T_1)$ ($4t_2 \rightarrow 5t_2$)	$\Delta + 4Dq + 12B - \epsilon(4t_2)$	43 374		0.0	

[a] Transition energies are calculated using the following set of parameters: $10Dq = 12\,000\ cm^{-1}$; $\Delta - \epsilon(1t_1) = 24\,200\ cm^{-1}$; $8B + 2C = E(1t_1,a^1E) - E(1t_1,^3A_2) = 6300\ cm^{-1}$, $\epsilon(1t_1) - \epsilon(4t_2) = E(4t_2,^3A_2) - E(1t_1,^3A_2) = 11\,200\ cm^{-1}$ ($C/B = 4.2$). [b] Calculated using the detailed prescription of ref 33 (see Appendix II) as well as MO coefficients for the antibonding 2e and $5t_2$ orbitals as supplied by the DFT results for MnO_4^{2-}: $\varphi(2e,u) = 0.8097d_{z^2} - 0.7578u_L$; $\varphi(5t_2,z) = -0.8491d_{xy} + 0.6494z_{\sigma}^{L} - 0.4983z_{\pi}^{L}$.

Turning to the d^1 oxo anions, we focus on MnO_4^{2-} (Cs_2SO_4), for which, in addition to the weak "d−d" band centered at 12 000 cm^{-1}, four nicely resolved CT bands (Figure 1a) have been reported.[10] Energy expressions, dipole matrix elements, and band assignments for the $d^1 \rightarrow d^2\underline{L}$ CT transitions are given in Table 6.[61] If, following section III.2, we assign the lowest LMCT1 band to a $1t_1 \rightarrow 2e$ transition, $^2E(d^1) \rightarrow {}^2T_2(1t_1,^3A_2)$, and take the corresponding energy expression $[\Delta - 6Dq - \epsilon(1t_1)]$ as a reference, the energies of all the other transitions can be expressed in terms of three parameters (eq 9). Using the expressions in Tables 6 and A2 (Appendix I)

$$E[1t_1,^1E(2e^2)] - E[1t_1,^3A_2(2e^2)] = 8B + 2C,\ C/B = 4.2$$

$$10Dq = E[^2T_2(d^1)] - E[^2E(d^1)] = 10Dq \qquad (9)$$

$$E[4t_2,^3A_2(2e^2)] - E[1t_1,^3A_2(2e^2)] = \epsilon(1t_1) - \epsilon(4t_2)$$

together with the definitions eq 9 we propose the following band assignment. The lowest excited CT state of MnO_4^{2-} at 17 000 cm^{-1} above the ground state corresponds to the ground state of the d^2 configuration, $^3A_2$ ($2e^2$), followed by $^1E(2e^2)$ at 23 300 cm^{-1}, both of which couple to a single hole in the nonbonding ligand orbital $1t_1$. Higher in energy, at 28 000 cm^{-1}, are the $^3T_2$ ($2e^15t_2^1$) and $^1A_1$ ($2e^2$) states of the d^2 shell, both combining with a single hole in the $1t_1$ orbital, and $^3A_2(2e^2)$ coupling with a hole in the $4t_2$ (cf. MO diagram in Figure 4). On the basis of the calculated oscillator strengths (Table 6), the CT band at 28 000 cm^{-1} can be assigned to this latter transition, $^2E \rightarrow {}^2T_1(4t_2,^3A_2)$, consistent with polarized single crystal absorption data.[62] Finally, the band at 34 200 cm^{-1} is attributed to the $^1E(2e^2)$ state coupling with a hole in the $4t_2$ orbital. The value of the energy difference $\epsilon(1t_1) - \epsilon(4t_2)$ resulting from our analysis, 11 200 cm^{-1} is very close to the DFT result (11 743 cm^{-1}). It is interesting to compare the $10Dq$ and B values for the $d^2\underline{L}$ final states deduced from the CT spectra of MnO_4^{2-} ($10Dq = 12\,000\ cm^{-1}$, $B = 384\ cm^{-1}$) with those of the corresponding d^2 complex MnO_4^{3-} ($10Dq = 10\,650\ cm^{-1}$, $B = 430\ cm^{-1}$ [54]). With one hole in nonbonding $1t_1$ or $4t_2$ orbitals, it is expected that, provided that other factors are equal, metal−ligand bonding for the d^2 and the $d^2\underline{L}$ systems will be essentially the same. However the Mn^{VI}−O and Mn^{V}−O bond lengths in the ground state are $R_{ML} = 1.65$ and 1.70 Å, respectively, and this difference greatly affects the Franck−Condon transition energies. The decrease in bond length from Mn^{V}−O to Mn^{VI}−O is accompanied by a significant increase of $10Dq$ and reduction of B, indicating that the Mn^{VI}−O bond is more covalent. If we adopt a power law dependence ($R_{ML}{}^{-n}$) of $10Dq$ and B on the distance, n values equal to 4 for $10Dq$ and 3.8 for B result. It should be noted that, due to the higher $10Dq$ (lower B) values for $d^2\underline{L}$ (MnO_4^{2-}) compared to d^2 (MnO_4^{3-}), the $^3T_2(2e^15t_2^1\underline{L})$ and $^1E,{}^1A_1(2e^2\underline{L})$ states of MnO_4^{2-} shift to higher and lower energies, respectively, resulting in an increase in the $^3T_2 - {}^1E$ splitting from about 2200 cm^{-1} for MnO_4^{3-} [54] to 5000 cm^{-1} in MnO_4^{2-} ($d^2\underline{L}$).

For the Cr complexes a similar effect leads to an interesting situation. The $^3T_2(2e^15t_2^1)$ and $^1E(2e^2)$ states of CrO_4^{4-} (d^2) have been calculated close in energy with $^3T_2$ below ^1E. As a result, the $^3A_2 \rightarrow {}^1E$ is obscured by the stronger $^3A_2 \rightarrow {}^3T_2$ absorption.[1] From the trends found for Mn, we expect that, going to the $d^2\underline{L}$ CT configurations of CrO_4^{3-}, $^1E\underline{L}$ states will be lowered in energy relative to $^3T_2\underline{L}$ states. In line with this, the spectrum of CrO_4^{3-} displays two CT bands with maxima at 28 000 cm^{-1} (LMCT1) and 36 000 cm^{-1} (LMCT2), Figure 1a. An assignment of these bands to the $^2E \rightarrow {}^2T_2[1t_1,^3A_2(2e^2)]$ and $^2E \rightarrow {}^2T_{2[1]}[1t_1,^1E(2e^2)]$ transitions as for MnO_4^{2-} appears reasonable in view of their similar shapes in the spectra of

(61) In Table 6 only the diagonal elements of the energy expressions are given. The calculations were carried out using full configuration interaction, however.

(62) Brunold, T. C.; Güdel, H. U. *Inorg. Chem.* **1997**, *36*, 1946.

Table 7. Calculated and Experimental Values of Oscillator Strengths (f_{d-d}) of the $2e \rightarrow 5t_2$ (Formally d−d) Transitions for VO_4^{4-}, CrO_4^{3-}, and MnO_4^{2-}

f_{d-d}	VO_4^{4-}	CrO_4^{3-}	MnO_4^{2-}
calcd	0.000 04	0.000 3	0.000 4
exptl	0.000 03[a]	0.0022[a]	0.001[a]

[a] Reference 11.

MnO_4^{2-} and CrO_4^{3-} and the good correspondence between calculated and experimental Huang−Rhys parameters (see section III.2). 10*Dq* and *B* values calculated for CrO_4^{3-} (13 500 and 488 cm^{-1}) and CrO_4^{4-} (9100 and 560 cm^{-1} (ref 1)) show again a strong dependence on the metal−ligand bond distance (1.695 and 1.76 Å, respectively). If we adopt the same power dependences for 10*Dq* and *B* vs R_{ML} as for MnO_4^{2-}, R_{ML}^{-4} and $R_{ML}^{-3.8}$, a calculation of 10*Dq* and *B* is possible for the $d^2\underline{L}$ CT configurations of CrO_4^{3-} (R_{ML} = 1.695 Å) based on the values of 10*Dq* and *B* for CrO_4^{4-}; we obtain 10*Dq* = 10 600 cm^{-1} and *B* = 468 cm^{-1}. The value of *B* is in excellent agreement with the one deduced from the CT spectra. In contrast, the experimental 10*Dq* value of 13 500 cm^{-1} [63] is substantially larger than the calculated value of 10 578 cm^{-1}. In part this might be due to the small PO_4^{3-} site of the Li_3PO_4 host lattice. However, other factors associated with the lattice surroundings, not accounted for in the cluster approximation, will also play an important role. Further, JT coupling may also contribute to larger observed 10*Dq* values.[53]

The oscillator strengths of the d−d transition (f_{d-d}) for MnO_4^{2-}, CrO_4^{3-}, and VO_4^{4-}, calculated following refs 31 and 32 with the wave functions from the DFT calculations discussed above (see Appendix II), increase with increasing covalency from VO_4^{4-} to CrO_4^{3-} and MnO_4^{2-} in contrast to the $1t_1 \rightarrow 2e$ (LMCT1) CT bands, which show the opposite trend (Table 7). These trends are experimentally verified by VO_4^{4-} and MnO_4^{2-}, whereas the d−d intensity of CrO_4^{3-} is higher than expected (like 10*Dq* and the intensity of the LMCT1 band) from this correlation. We attribute these differences to influences from the host lattice. Nevertheless, these results indicate that the role of covalency is such as to provide intensity for d−d transitions via mixing with CT transitions, while ionicity, which tends to restrict this mixing, leads to an increase in intensity of $1t_1 \rightarrow 2e$ CT transitions in the opposite direction (i.e., from Mn to Cr and V).

IV. Conclusions

(1) Density functional theory (DFT) calculations on a series of tetrahedrally oxocoordinated d^0 ions and their d^1 analogues show that covalency of the metal−oxygen bond and delocalization of 3d electrons over ligand orbitals increase from V to Cr to Mn and, to a lesser extent, from the d^1 complexes to their d^0 analogues. Upon ligand-to-metal CT excitation the $1t_1 - 2e$ energy difference increases and the MOs of the 3d type become more localized on the metal.

(2) DFT calculated energies (in cm^{-1}) of the lowest $1t_1 \rightarrow 2e$ CT transitions increase from MnO_4^- to CrO_4^{2-} and VO_4^{3-}, from MnO_4^{2-} to CrO_4^{3-} and VO_4^{4-}, and to a lesser extent from the d^0 to the d^1 oxo anions, in agreement with experimental data (Table 8). As exemplified by CrO_4^{2-} and VO_4^{3-}, effects of the surroundings in solids or ionic solutions can lead to large variations in the CT energy for a given ion, shown by recent Hartree−Fock and MCSCF calculations[7] to be due to Madelung effects.

Table 8. DFT Calculated and Experimental Energies of the Lowest $1t_1 \rightarrow 2e$ CT Transition in the d^0, MnO_4^-, CrO_4^{2-}, and VO_4^{3-} and d^1, MnO_4^{2-}, CrO_4^{3-} and VO_4^{4-} Oxo Anions[a]

	MnO_4^-	CrO_4^{2-}	VO_4^{3-}
calcd	19 082	27 167	37 827
exptl	19 000 [$KMnO_4$][b]	28 000 [K_2CrO_4][c]	39 500 [Ca_2PO_4Cl][e]
		27 000 [$CdSO_4$][d]	36 500 [1 M NaOH, H_2O sol.] [f]
			24 000 [V, Al:SiO_2][g]

	MnO_4^{2-}	CrO_4^{3-}	VO_4^{4-}
calcd	20 653	30 475	44 687
exptl	17 000 [Cs_2SO_4][h]	28 000 [Li_3PO_4][h]	

[a] Host matrix indicated in square brackets. [b] Reference 12. [c] Reference 13. [d] Reference 59. [e] Reference 14. [f] Reference 51. [g] Reference 52. [h] Reference 11.

Table 9. 10*Dq* and *B* Parameters (in cm^{-1}) vs Ground State Metal−Oxygen Bond Distances R_{ML} (in Å) for the d^1 (MnO_4^{2-}, CrO_4^{3-}), d^2 (MnO_4^{3-} and CrO_4^{4-}), and d^0 (MnO_4^- and CrO_4^{2-}) Oxo Anions, Deduced from d−d (for d^1 and d^2) Ligand Field and $d^2\underline{L}$(for d^1) and $d^1\underline{L}$(for d^0) CT Spectra

	MnO_4^- ($d^1\underline{L}$)	MnO_4^{2-}($d^2\underline{L}$)	MnO_4^{3-} (d^2)
10*Dq*	14 000 [$KMnO_4$][a]	12 000 [Cs_2MnO_4][a]	10650 [Sr_2VO_4Cl][b]
B		384[a]	430[b]
R_{ML}	1.629[e]	1.659 [f]	1.700[g]

	CrO_4^{2-} ($d^1\underline{L}$)	CrO_4^{3-} ($d^2\underline{L}$)	CrO_4^{4-} (d^2)
10*Dq*	14 640 [$CdSO_4$][a]	13 500 [Li_3PO_4][a]	8 950 [Ca_2GeO_4][d]
		12 500 [Sr_2VO_4Cl][c]	10 100 [Mg_2SiO_4][d]
B		488[a]	560[d]
R_{ML}	1.66[i]	1.695[c]	1.76 [j]

[a] This work. [b] Reference 54. [c] Reference 45. [d] Reference 1. [e] Reference 43. [f] Reference 46. [g] Reference 53. [i] Reference 42. [j] Liu, G.; Greedan, J. E.; Gong, W. *J. Solid State Chem.* **1993**, *105*, 78.

(3) The configuration interaction model introduced in section II.2. permits a detailed analysis of the ligand-to-metal CT spectra of the d^1 and d^0 oxo anions in terms of the corresponding $d^2\underline{L}$ and $d^1\underline{L}$ multiplets, respectively. 10*Dq* values and Racah *B* parameters for the d^1 ions in their $d^2\underline{L}$ CT excited states are larger and smaller, respectively, than for the d^2 ions (Table 9). This reflects an increase in metal−ligand covalency (reduction of *B*) and bond strength (increase in 10*Dq*) when lowering the number of antibonding d electrons from d^2 to d^1 and d^0. A comparison between DFT calculated and experimental 10*Dq* values shows that in some cases this correlation is not fulfilled. This is due to the strong dependence of 10*Dq* on the host lattice (ionic surroundings), which is not always reflected by the metal−ligand bond distance variations.

(4) From a comparison of the metal−oxygen bond distances obtained from DFT geometry optimizations for $d^1\underline{L}$ CT configurations of the d^0 anions and those calculated for the ground ^2E and $^2T_2$ LF excited states of the d^1 anions, an essential contribution of the ionic charges and their interactions to the metal−ligand bond is deduced. In addition to the pure antibonding effect due to occupancy of the metal "3d" MOs, the reduction of the metal and ligand charges upon ligand-to-metal CT excitation also contributes to a lengthening of the metal−ligand bond. This effect becomes stronger with increasing ionicity from Mn to Cr to V and may be responsible for the increase of the Huang−Rhys parameters and intensities of the CT absorption bands from MnO_4^{2-}, to CrO_4^{3-} and VO_4^{4-}. For d−d transitions, an opposite effect is theoretically predicted and experimentally observed for MnO_4^{2-} and VO_4^{4-}; with increasing

(63) Hazenkamp, M. F.; Güdel, H. U. *Chem. Phys. Lett.* **1996**, *251*, 301.

Table A1. Symmetry-Adapted $^2T_2$ and $^2T_1$ (in Square Brackets) Functions for Holes, Resulting from $d^8\underline{L}$ {$\underline{L}$-Ligand Hole; d = $2e[u(d_{z^2}),v(d_{x^2-y^2})]$, $5t_2[k(d_{yz}),e(d_{xz}),z(d_{xy})]$ and $\underline{L} = 1t_1(a,b,g)$, $4t_2(k_L,e_L,z_L)$} Singly Excited CT Configurations for d^1 (Nine Holes) MO_4^z Oxo Anions (M, z = Mn, −2; Cr, −3; V, −4)

coupling $\underline{L} - d^8$	wave functions[a]
$1t_1,^3A_2$	$(1/\sqrt{3})\|g,1/2\rangle\|^3A_2,0\rangle - \sqrt{(2/3)}\|g,-1/2\rangle\|^3A_2,1\rangle$
$4t_2,^3A_2$	$[-(1/\sqrt{3})\|z_L,1/2\rangle\|^3A_2,0\rangle + \sqrt{(2/3)}\|z_L,-1/2\rangle\|^3A_2,1\rangle]$
$1t_{1,a,b}{}^1E$	$-\|g,1/2\rangle_{\|a,b}{}^1E,v\rangle[\|g,1/2\rangle_{\|a,b}{}^1E,u\rangle]$
$4t_{2,a,b}{}^1E$	$\|z_L,1/2\rangle_{\|a,b}{}^1E,u\rangle[\|z_L,1/2\rangle_{\|a,b}{}^1E,v\rangle]$
$4t_{2,a,b}{}^1A_1$	$\|z_L,1/2\rangle_{\|a,b}{}^1A_1\rangle[\|g,1/2\rangle_{\|a,b}{}^1A_1\rangle]$
$1t_1,^3T_2$	$-[+](1/\sqrt{6})\|a,1/2\rangle\|^3T_2,e,0\rangle + [-](1/\sqrt{3})\|a,-1/2\rangle\|^3T_2,e,1\rangle + (1/\sqrt{6})\|b,1/2\rangle\|^3T_2,k,0\rangle - (1/\sqrt{3})\|b-1/2\rangle\|^3T_2,k,1\rangle$
$4t_2,^3T_2$	$(1/\sqrt{6})\|k_L,1/2\rangle\|^3T_2,e,0\rangle - (1/\sqrt{3})\|k_L,-1/2\rangle\|^3T_2,e,1\rangle + [-](1/\sqrt{6})\|e_L,1/2\rangle\|^3T_2,k,0\rangle - [+](1/\sqrt{3})\|e_L,-1/2\rangle\|^3T_2,k,1\rangle$
$1t_{1,a,b}{}^3T_1$	$-(1/\sqrt{6})\|a,1/2\rangle_{\|a,b}{}^3T_1,b,0\rangle + (1/\sqrt{3})\|a,-1/2\rangle_{\|a,b}{}^3T_1,b,1\rangle - [+](1/\sqrt{6})\|b,1/2\rangle_{\|a,b}{}^3T_1,a,0\rangle + [-](1/\sqrt{3})\|b,-1/2\rangle_{\|a,b}{}^3T_1,a,1\rangle$
$4t_{2,a,b}{}^3T_1$	$-[+](1/\sqrt{6})\|e_L,1/2\rangle_{\|a,b}{}^3T_1,a,0\rangle + [-](1/\sqrt{3})\|e_L,-1/2\rangle_{\|a,b}{}^3T_1,a,1\rangle + (1/\sqrt{6})\|k_L,1/2\rangle_{\|a,b}{}^3T_1,b,0\rangle - (1/\sqrt{3})\|k_L,-1/2\rangle\|^3T_1,b,1\rangle$
$1t_1,^1T_1$	$-(1/\sqrt{2})\|a,1/2\rangle\|^1T_1,b\rangle$-$[+](1/\sqrt{2})\|b,1/2\rangle\|^1T_1,a\rangle$
$4t_2,^1T_1$	$-[+](1/\sqrt{2})\|e_L,1/2\rangle\|^1T_1,a\rangle + (1/\sqrt{2})\|k_L,1/2\rangle\|^1T_1,b\rangle$
$1t_{1,a,b}{}^1T_2$	$-[+](1/\sqrt{2})\|a,1/2\rangle_{\|a,b}{}^1T_2,e\rangle + (1/\sqrt{2})\|b,1/2\rangle_{\|a,b}{}^1T_2,k\rangle$
$4t_{2,a,b}{}^1T_2$	$(1/\sqrt{2})\|k_L,1/2\rangle_{\|a,b}{}^1T_2,e\rangle + [-](1/\sqrt{2})\|e_L,1/2\rangle_{\|a,b}{}^1T_2,k\rangle$

[a] Functions for one and eight holes are denoted by $|\gamma,m_s>$ and $|^{2S+1}\Gamma,\gamma,M_s>$ respectively; $m_s = 1/2$, M_s (z component for nonzero S), Γ (irreducible representation), γ (component).

covalency the intensity of d−d transitions increases due to mixing with CT transitions.

Acknowledgment. This work was supported by a research grant (to M.A.) from the Swiss National Science Foundation and the Hans-Sigrist Foundation. One of us (M.A.) is grateful to Raf Bruyndonckx, Fribourg, Switzerland, for his help with the ADF computations.

Appendix I

Since the number of holes (10 for the d^0 and 9 for the d^1 system) is less than the number of electrons, we use a hole formalism. In the ground state the ligand orbitals are lower and doubly occupied with electrons, while for holes they are empty and higher in energy than the metal orbitals. The ground states for the d^{10} and d^9 systems are described by the $^1A_1$ and ^2E terms with wave functions

$$|^1A_1\rangle = |u_\alpha u_\beta v_\alpha v_\beta k_\alpha k_\beta e_\alpha e_\beta z_\alpha z_\beta| \quad \text{(A.1)}$$

$$|^2E,u,\alpha\rangle = -|u_\alpha v_\alpha v_\beta k_\alpha k_\beta e_\alpha e_\beta z_\alpha z_\beta||^2E,u,\beta\rangle = -|u_\beta v_\alpha v_\beta k_\alpha k_\beta e_\alpha e_\beta z_\alpha z_\beta|$$

$$|^2E,v,\alpha\rangle = -|u_\alpha u_\beta v_\alpha k_\alpha k_\beta e_\alpha e_\beta z_\alpha z_\beta||^2E,v,\beta\rangle = -|u_\alpha u_\beta v_\beta k_\alpha k_\beta e_\alpha e_\beta z_\alpha z_\beta| \quad \text{(A.2)}$$

Wave functions for the $^2T_2$ ligand field excited state for d^9 (electronic d^1) are

$$|^2T_2,k,\alpha\rangle = -|u_\alpha u_\beta v_\alpha v_\beta k_\alpha e_\alpha e_\beta z_\alpha z_\beta||^2T_2,k,\beta\rangle = -|u_\alpha u_\beta v_\alpha v_\beta k_\beta e_\alpha e_\beta z_\alpha z_\beta|$$

$$|^2T_2,e,\alpha\rangle = -|u_\alpha u_\beta v_\alpha v_\beta k_\alpha k_\beta e_\alpha z_\alpha z_\beta||^2T_2,e,\beta\rangle = -|u_\alpha u_\beta v_\alpha v_\beta k_\alpha k_\beta e_\beta z_\alpha z_\beta| \quad \text{(A.3)}$$

$$|^2T_2,z,\alpha\rangle = -|u_\alpha u_\beta v_\alpha v_\beta k_\alpha k_\beta e_\alpha e_\beta z_\alpha||^2T_2,z,\beta\rangle = -|u_\alpha u_\beta v_\alpha v_\beta k_\alpha k_\beta e_\alpha e_\beta z_\beta|$$

and for the L → M ($d^9\underline{L}$) CT states

$$|^1T_2,z(^2E1t_1)\rangle = (1/\sqrt{2})[-|^2E,v,\alpha\rangle|1t_1,g,\beta\rangle + |^2E,v,\beta\rangle|1t_1,g,\alpha\rangle]$$

$$|^1T_2,z(^2E4t_2)\rangle = (1/\sqrt{2})[|^2E,u,\alpha\rangle|4t_2,z_L,\beta\rangle - |^2E,u,\beta\rangle|4t_2,z_L,\alpha\rangle] \quad \text{(A.4)}$$

$$|^1T_2,z(^2T_21t_1)\rangle = (1/2)[-|^2T_2,e,\alpha\rangle|1t_1,a,\beta\rangle + |^2T_2,e,\beta\rangle|1t_1,a,\alpha\rangle + |^2T_2,k,\alpha\rangle|1t_1,b,\beta\rangle - |^2T_2,k,\beta\rangle|1t_1,b,\alpha\rangle]$$

$$|^1T_2,z(^2T_24t_2)\rangle = (1/2)[|^2T_2,k,\alpha\rangle|4t_2,e_L,\beta\rangle - |^2T_2,k,\beta\rangle|4t_2,e_L,\alpha\rangle + |^2T_2,e,\alpha\rangle|4t_2,k_L,\beta\rangle - |^2T_2,e,\beta\rangle|4t_2,k_L,\alpha\rangle]$$

In eq A.4 only z components of each $^1T_2$ term are given. u, v and k, e, z denote the antibonding MOs transforming as the d_{z^2}, $d_{x^2-y^2}$ (2e) and d_{yz} (ξ), d_{xz} (η) and d_{xy} (ζ) ($5t_2$), while α and β denote the $|s,m_s\rangle$ spin functions, $|^1/_2,^1/_2\rangle$ and $|^1/_2,-^1/_2\rangle$, respectively. The symbols a,b,g ($1t_1$) and k_L,e_L,z_L ($4t_2$) denote ligand 2p MOs which transform as rotations R_x, R_y, R_z and translations T_x, T_y, T_z, respectively.

Symmetry-adapted functions for singly excited ($d^8\underline{L}$) $^2T_2$ and $^2T_1$ CT states in the d^9 (electronic d^1) T_d clusters are derived in two steps; in a first step, symmetry-adapted functions for eight holes are constructed as complementary to functions for two electrons in the antibonding $2e[u(d_{z^2}), v(d_{x^2-y^2})]$ and $5t_2[k(d_{yz}),e(d_{xz}),z(d_{xy})]$ "3d" orbitals. In a second step, singlet and triplet functions for d^8 are coupled with one hole on the ligand $1t_1$-(a,b,g) and $4t_2(k_L,e_L,z_L)$ orbitals to obtain wave functions with a total spin $S = ^1/_2$ and space symmetries T_2 and T_1. Wigner and Clebsch-Gordon coefficients for spin and space functions, respectively, are those from ref 64. For a list of all spin- and symmetry-adapted $^2T_2$ and $^2T_1$ functions of the $d^8\underline{L}$ configuration, see Table A1. The Hamiltonian is written in terms of the spin (σ) and orbital (i) creation ($a_{i\sigma}{}^+$) and annihilation ($a_{i\sigma}$) operators for holes in the i = 2e, $5t_2$, $1t_1$, $4t_2$ orbitals (for the single-particle terms) and for d orbitals (i, j, k, l = 2e and $5t_2$,

(64) Sugano, S.; Tanabe, Y.; Kamimura, H. *Multiplets of Transition Metal Ions in Crystals*; Academic Press: New York, 1970.

Table A2. Matrix Elements of the CICT Model Hamiltonian and the Dipole Operator (z Component, P_z) for Transitions from the ^2E Ground State of a Tetrahedral d^1 (Nine Holes) Transition Metal Cluster, Including the Ligand Field ($^2T_2$) and the Singly Excited ($d^8\underline{L}$,$\underline{L}$-Ligand Hole) Ligand-to-Metal CT States [$^2T_2$ and $^2T_1$ (in Square Brackets)][a]

no.	term	diagonal energy expression[b]	$\langle ^2T_{2[1]}\|P_z\|^2E(d^9)\rangle$
1	$^2E(2e^3 5t_2^6)$	$-6Dq$	
2	$^2T_2(2e^4 5t_2^5)$	$4Dq$	$\langle u\|z\rangle$[c]
3	$^2T_{2[1]}(1t_1[4t_2],^3A_2)$	$\Delta - 12Dq - \epsilon(1t_1[4t_2])$	$(3/\sqrt{6})\langle v\|g\rangle[(3/\sqrt{6})\langle u\|z_L\rangle]$
4	$^2T_{2[1]}(1t_{1,a},^1E)$	$\Delta - 12Dq + 8B + 2C - \epsilon(1t_1)$	$-[+]\langle v\|g\rangle$
5	$^2T_{2[1]}(1t_{1,b},^1E)$	$\Delta + 8Dq + 9B + 2C - \epsilon(1t_1)$	0
6	$^2T_{2[1]}(4t_{2,a},^1E)$	$\Delta - 12Dq + 8B + 2C - \epsilon(4t_2)$	$-[+](1/\sqrt{2})\langle u\|z_L\rangle$
7	$^2T_{2[1]}(4t_{2,b},^1E)$	$\Delta + 8Dq + 9B + 2C - \epsilon(4t_2)$	0
8	$^2T_{2[1]}(4t_2[1t_1],_a{}^1A_1)$	$\Delta - 12Dq + 16B + 4C - \epsilon(4t_2[1t_1])$	$(1/\sqrt{2})\langle u\|z_L\rangle[(1/\sqrt{2})\langle v\|g\rangle]$
9	$^2T_{2[1]}(4t_2[1t_1],_b{}^1A_1)$	$\Delta + 8Dq + 18B + 5C - \epsilon(4t_2[1t_1])$	0
10	$^2T_{2[1]}(1t_1,^3T_2)$	$\Delta - 2Dq - \epsilon(1t_1)$	$(\sqrt{3}/2)[-3/2]\langle k\|b\rangle$
11	$^2T_{2[1]}(4t_2,^3T_2)$	$\Delta - 2Dq - \epsilon(4t_2)$	$(\sqrt{3}/2)[3/2]\langle e\|k_L\rangle$
12	$^2T_{2[1]}(1t_{1,a},^3T_1)$	$\Delta - 2Dq + 12B - \epsilon(1t_1)$	$(-3/2)[\sqrt{3}/2]\langle k\|b\rangle$
13	$^2T_{2[1]}(1t_{1,b},^3T_1)$	$\Delta + 8Dq + 3B - \epsilon(1t_1)$	0
14	$^2T_{2[1]}(4t_{2,a},^3T_1)$	$\Delta - 2Dq + 12B - \epsilon(4t_2)$	$(-3/2)[\sqrt{3}/2]\langle e\|k_L\rangle$
15	$^2T_{2[1]}(4t_{2,b},^3T_1)$	$\Delta + 8Dq + 3B - \epsilon(4t_2)$	0
16	$^2T_{2[1]}(1t_1,^1T_1)$	$\Delta - 2Dq + 12B + 2C - \epsilon(1t_1)$	$(\sqrt{3}/2)[-1/2]\langle k\|b\rangle$
17	$^2T_{2[1]}(4t_2,^1T_1)$	$\Delta - 2Dq + 12B + 2C - \epsilon(4t_2)$	$(\sqrt{3}/2)[-1/2]\langle e\|k_L\rangle$
18	$^2T_{2[1]}(1t_{1,a},^1T_2)$	$\Delta - 2Dq + 8B + 2C - \epsilon(1t_1)$	$(-1/2)[\sqrt{3}/2]\langle k\|b\rangle$
19	$^2T_{2[1]}(1t_{1,b},^1T_2)$	$\Delta + 8Dq + 9B + 2C - \epsilon(1t_1)$	0
20	$^2T_{2[1]}(4t_{2,a},^1T_2)$	$\Delta - 2Dq + 8B + 2C - \epsilon(4t_2)$	$(-1/2)[-\sqrt{3}/2]\langle e\|k_L\rangle$
21	$^2T_{2[1]}(4t_{2,b},^1T_2)$	$\Delta + 8Dq + 9B + 2C - \epsilon(4t_2)$	0

[a] Notations of molecular orbital components: $k(d_{yz})$, $e(d_{xz})$, $z(d_{xy})$ for $5t_2(3d)$, $u(d_{z^2})$, $v(d_{x^2-y^2})$ for $2e(3d)$, a, b, g for $1t_1$, and k_L, e_L, z_L for $4t_2$. [b] Off-diagonal matrix elements are $(4|5) = (6|7) = -(18|19) = -(20|21\rangle = -2\sqrt{3}B$; $(8|9) = \sqrt{6}(2B + C)$; $(12|13) = (14|15) = 6B$. [c] For notations of the dipole matrix elements see text.

for the two-particle Coulomb repulsion term):

$$H = \sum_i t_{ii} a_{i\sigma}{}^+ a_{i\sigma} + (1/2)\sum_{ij,kl} U_{ij,kl} a_{i\sigma}{}^+ a_{j\sigma'}{}^+ a_{l\sigma'} a_{k\sigma} \qquad \text{(A.5)}$$

$$U_{ij,kl} = \int\int \varphi_i{}^*(1)\, \varphi_j{}^*(2)(1/r_{12})\, \varphi_k(1)\, \varphi_l(2)\, d\tau_1\, d\tau_2 \qquad \text{(A.6)}$$

It should be noted that the operator H is written in a MO basis which allows one to avoid mixed products in the first term of eq A.5. The orbital parameter t_{ii} for orbitals $i = 5t_2$, 2e, $1t_1$, and $4t_2$ can be identified with the orbital energies $-\delta - 4Dq$, $-\delta + 6Dq$, $-\epsilon(1t_1)$, and $-\epsilon(4t_2)$, respectively (see Figure 3, but with an opposite sign). The Coulomb repulsion terms $U_{ij,kl}$ can be expressed in terms of the Racah parameters A, B, and C (see ref 64). Since molecular instead of atomic orbitals are used, the parameters A, B, and C (and correspondingly $U_{ij,kl}$) are reduced with respect to their values for free ions. Applying the operator H on the basis functions in Table A1 yields, in combination with eq 5, diagonal and off-diagonal matrix elements listed in Table A2 along with the matrix elements of the dipole operator (P_z).

Appendix II

The matrix elements of the electric dipole transition moment operator (**P**) for transitions between a nonbonding ligand orbital ($\chi_{nb} = 1t_1$, $4t_2$) and an antibonding $\varphi = a(3d) - b(\chi)$ orbital ($\varphi = 2e$, $5t_2$) consists of two contributions: ligand−metal, $\langle 3d|\mathbf{r}|\chi_{nb}\rangle$ and ligand−ligand $\langle\chi|\mathbf{r}|\chi_{nb}\rangle$. If overlap of 2p orbitals is neglected, the $\langle\chi|\mathbf{r}|\chi_{nb}\rangle$ term is approximated as described in ref 35 and calculated using the explicit forms of the $1t_1$, $4t_2$, 2e and $5t_2$ orbitals from DFT calculations. Utilizing the cubic symmetry, only matrix elements for z components of **P** (P_z) are calculated, P_x and P_y yielding contributions of the same magnitude. Following ref 34, $P_z = ez$ is projected onto the local frame of a given ligand x_L,y_L,z_L (for definition of ligand coordinates in T_d symmetry, see ref 65) with ligand functions p_z and p_x,p_y, which are appropriately aligned (for σ and π overlap, respectively) with the metal orbitals. The products of the P_z components in the local ligand frame (x_L,y_L,z_L) and the ligand functions p_x,p_y,p_z can be represented as linear combinations of 3d and 3s, ligand-centered orbitals with the same exponents (ζ_{2p}) as 2p:

$$y_L\, p_z = z_L\, p_y = (\sqrt{6}/2)(a_0/\zeta_{2p})d_{yz}{}^L$$

$$x_L\, p_z = z_L\, p_x = (\sqrt{6}/2)(a_0/\zeta_{2p})d_{xz}{}^L$$

$$x_L\, p_y = y_L\, p_x = (\sqrt{6}/2)(a_0/\zeta_{2p})d_{xy}{}^L \qquad \text{(A.7)}$$

$$z_L\, p_z = \sqrt{2}(a_0/\zeta_{2p})d_{z^2}{}^L + (\sqrt{10}/2)(a_0/\zeta_{2p})3s^L$$

$$y_L\, p_y = -(\sqrt{6}/2)(a_0/\zeta_{2p})d_{x^2-y^2}{}^L + (\sqrt{2}/2)(a_0/\zeta_{2p})d_{z^2}{}^L + (\sqrt{10}/2)(a_0/\zeta_{2p})3s^L$$

$$x_L\, p_x = (\sqrt{6}/2)(a_0/\zeta_{2p})d_{x^2-y^2}{}^L - (\sqrt{2}/2)(a_0/\zeta_{2p})d_{z^2}{}^L + (\sqrt{10}/2)(a_0/\zeta_{2p})3s^L$$

Thus, using eq A.7, matrix elements of the type $\langle 3d|P_z|2p\rangle$ are reduced to standard overlap integrals between metal $3d(\zeta_{3d})$ and ligand $3d(\zeta_{2p})$,$3s(\zeta_{2p})$ orbitals. Employing explicit formulas for ligand $1t_1$,$t_2(\sigma)$ and $t_2(\pi)$ functions (for their definition see ref 65) we derive the (nonzero) matrix elements (eq A.8, in Å, a_0

Table A3. Experimental and Calculated (Including Ligand−Metal, $\langle 3d|\mathbf{r}|\chi_{nb}\rangle$ and Ligand−Ligand $\langle\chi|\mathbf{r}|\chi_{nb}\rangle$ Terms) Oscillator Strengths (f) of the Lowest $1t_1 \rightarrow 2e$ CT Transition in d^0 Oxo Anions MnO_4^-, CrO_4^{2-}, and VO_4^{3-}

	MnO_4^-	CrO_4^{2-}	VO_4^{3-}
f (exptl)[a]	0.032	0.089	0.150
$f(\langle 3d\|\mathbf{r}\|\chi_{nb}\rangle)$	0.010	0.017	0.026
$f(\langle\chi\|\mathbf{r}\|\chi_{nb}\rangle)$	0.636	0.774	0.916

[a] Reference 11.

(65) Ballhausen, C. J.; Gray, H. B. *Molecular Orbital Theory, An Introductory Lecture Note and Reprint Volume*; Benjamins: New York, Amsterdam, 1965.

Table A4. MO Coefficients and Dipole Operator (P_z) Matrix Elements for Oscillator Strengths of "d−d" Transitions in d^1 Tetrahedral Oxo Anions

	a_d	a_π	b_d	b_σ	b_π	$\langle z\|u_L\rangle$	$\langle u\|z_\sigma^L\rangle$	$\langle u\|z_\pi^L\rangle$
MnO_4^{2-}	0.8097	−0.7578	−0.8491	0.6494	−0.4983	0.0989	−0.1199	0.0848
CrO_4^{3-}	0.8873	−0.6824	−0.9315	0.5837	−0.4723	0.1300	−0.1345	0.0951
VO_4^{4-}	0.9663	−0.6008	−1.0039	0.4889	−0.4612	0.1672	−0.1417	0.1002

= 0.529 Å, the Bohr radius). DFT calculations show that to a good approximation the upper ligand orbital of t_2 symmetry is represented as

$$\langle u|z|z_\sigma^{L}\rangle = 2\sqrt{(2/3)}(a_0/\zeta_{2p})S_{d_\pi d_\pi}(\zeta_{3d},\zeta_{2p})$$

$$\langle u|z|z_\pi^{L}\rangle = -(2/\sqrt{3})(a_0/\zeta_{2p})S_{d_\pi d_\pi}(\zeta_{3d},\zeta_{2p})$$

$$\langle v|z|g\rangle = (2/\sqrt{3})(a_0/\zeta_{2p})S_{d_\pi d_\pi}(\zeta_{3d},\zeta_{2p}) \qquad (A.8)$$

$$\langle k|z|e_\sigma^{L}\rangle = [(\sqrt{2/3})S_{d_\pi d_\pi}(\zeta_{3d},\zeta_{2p}) + (2\sqrt{2/3})S_{d_\sigma d_\sigma}(\zeta_{3d},\zeta_{2p}) + (\sqrt{10/3})S_{d_\sigma,s}(\zeta_{3d},\zeta_{2p})](a_0/\zeta_{2p})$$

$$\langle k|z|e_\pi^{L}\rangle = [-(1/3)(S_{d_\pi d_\pi}(\zeta_{3d},\zeta_{2p}) + S_{d_\sigma d_\sigma}(\zeta_{3d},\zeta_{2p})) + (\sqrt{5/3})S_{d_\sigma,s}(\zeta_{3d},\zeta_{2p})](a_0/\zeta_{2p})$$

$$\langle k|z|b\rangle = [(1/\sqrt{3})(S_{d_\pi d_\pi}(\zeta_{3d},\zeta_{2p}) - S_{d_\sigma d_\sigma}(\zeta_{3d},\zeta_{2p})) + (\sqrt{15/3})S_{d_\sigma,s}(\zeta_{3d},\zeta_{2p})](a_0/\zeta_{2p})$$

$$\langle z|u_L\rangle = [-(2/3)(S_{d_\pi d_\pi}(\zeta_{3d},\zeta_{2p}) + S_{d_\sigma d_\sigma}(\zeta_{3d},\zeta_{2p})) + (2\sqrt{5/3})S_{d_\sigma,s}(\zeta_{3d},\zeta_{2p})](a_0/\zeta_{2p})$$

$$t_2 = -(2/\sqrt{6})t_2(\pi) + (1/\sqrt{3})t_2(\sigma) \qquad (A.9)$$

Using eqs A.8 and A.9, dipole matrix elements have been computed for the d^0 and d^1 anions using Slater exponents [1.925 (ζ_{2p} for O^{2-}) and 1.667 (V^V and V^{IV}), 2.000 (Cr^{VI} and Cr^V), and 2.333 (Mn^{VII} and Mn^{VI}) for ζ_{3d}] and M−O distances (all in Å) of 1.71 (1.76) [V^V (V^{IV})], 1.66 (1.693) [Cr^{VI} (Cr^V)], 1.629 (1.659) [Mn^{VII} (Mn^{VI})]. Substituting $\langle 3d|P_z|2p\rangle$ (A.8) in eq 5 and Table A2, oscillator strengths are calculated (eq A.10, $h\nu$ = the transition energy in cm^{-1}).

$$f = (1.085 \times 10^{-5})h\nu 3|\langle 3d|P_z|2p\rangle|^2 \qquad (A.10)$$

Values of f for the $1t_1 \rightarrow 2e$ CT transition of the d^0 oxo anions corresponding to the $\langle 3d|\mathbf{r}|\chi_{nb}\rangle$ and $\langle \chi|\mathbf{r}|\chi_{nb}\rangle$ terms are respectively smaller and much larger than the experimental ones (Table A3). However, both sets of calculations lead to the same experimental trend.

Considering d−d transitions, 2e and $5t_2$ can be written as (contributions of oxygen 2s orbitals are neglected here)

$$\varphi(2e,u) = a_d u(3d) + a_\pi u_L$$

$$\varphi(5t_2,z) = b_d z(3d) + b_\sigma z_\sigma^{L} + b_\pi z_\pi^{L} \qquad (A.11)$$

to give the following expression for the matrix element $\langle u|z\rangle$ (Table A2):

$$\langle u|z\rangle \equiv \langle u|P_z|z\rangle = b_d a_\pi \langle z|u_L\rangle + a_d b_\sigma \langle u|z_\sigma^{L}\rangle + a_d b_\pi \langle u|z_\pi^{L}\rangle \qquad (A.12)$$

In calculating (f) for "d−d" transitions, use is made of the explicit forms of 2e and $5t_2$ MOs as obtained from DFT calculations and dipole matrix elements as given in Table A4.

IC971014H